Astron. Astrophys. 332, 429–448 (1998)

ASTRONOMY AND ASTROPHYSICS

# Expanding HI shells in NGC 2403

## First results from an automated object recognition package

**David A. Thilker**[1], **Robert Braun**[2], **and René A.M. Walterbos**[1,⋆]

[1] Department of Astronomy, New Mexico State University Box 30001/Department 4500, Las Cruces, NM 88003-8001, USA
[2] Netherlands Foundation for Research in Astronomy P.O. Box 2, 7990 AA Dwingeloo, The Netherlands

Received 14 April 1997 / Accepted 13 October 1997

**Abstract.** We have developed an automated package of object recognition software to detect and accurately characterize expanding HI supershells in nearby spiral galaxies. Our method avoids the ambiguity associated with visually identifying complex, expanding structures in spectral line datacubes. In this pilot study, an analytic expression for the time evolution of a supershell is used to derive the approximate structure of a parameterized shell expanding inside a plane-stratified gaseous disk. The resulting model is projected spatially and in velocity to determine an "observable" signature for the expanding structure. We then cross-correlate an observed HI datacube with an ensemble of these 3-dimensional filter kernels, which specify the predicted appearance of shells having different sizes and expansion velocities. Processed datacubes often contain correlation peaks of statistical significance, regions in which observed emission matches the appearance of a model supershell. To demonstrate our automated package, we describe properties of 50 high quality supershells in NGC 2403, comprising $2.1\times10^8$ $M_\odot$ of HI and at least $2.2\times10^{54}$ ergs of kinetic energy. We are analyzing 20 other galaxies with our object recognition software, looking for variation in supershell characteristics as a function of Hubble type and star formation rate.

**Key words:** galaxies: individual (NGC 2403) – galaxies: ISM – ISM: bubbles – ISM: kinematics and dynamics – methods: data analysis – radio lines: galaxies

### 1. Introduction

In several nearby spiral galaxies, the diffuse interstellar medium (ISM) appears to host scores of expanding gaseous shells. Energy supplied to the ISM by massive stars via strong stellar winds, ionizing radiation, and supernovae (SNe) is commonly regarded as a plausible power source for the creation of these structures (Tomisaka 1992, Tenorio-Tagle et al. 1990, Mac Low et al. 1989, Norman & Ikeuchi 1989). A limited number of extraordinary cases seem to require a more energetic mechanism such as high-velocity clouds (HVCs) impacting with the disk (Rand & Stone 1996, Rand & van der Hulst 1993, Tenorio-Tagle & Bodenheimer 1988, Tenorio-Tagle et al. 1987). Although the characteristics of most gaseous shells are consistent with creation via one of these modes, fine details of supershell evolution remain unclear.

We adopt the hypothesis that massive stars create most superbubbles. If this is true, the observed supershell population is an important gauge of the cyclic relationship between the gaseous and stellar components in spiral galaxies. Details of this cycle will clearly affect how galaxies evolve and are important to understand.

Large-scale expanding HI shells were first detected in the Magellanic Clouds, over three decades ago. Early observations from the Parkes radio telescope revealed a handful of superbubbles in both the LMC (Westerlund & Mathewson 1966, McGee & Milton 1966) and SMC (Hindman 1967, references therein). Numerous expanding structures were later discovered in the Galaxy by Heiles (1976, 1979), highlighting the importance of this research topic. Brinks and Bajaja (1986) pioneered the study of supershells in spiral galaxies other than the Milky Way, completing a survey for "HI holes" in M31. This work opened the door for several investigations of a similar nature during the subsequent decade. Deul & den Hartog (1990) compiled a list of superbubbles in M33, identifying a tendency for small shells to correlate with OB associations and larger structures to be surrounded by compact HII regions. While analyzing a high-resolution survey of Holmberg II (a dwarf companion to M81), Puche et al. (1992) pointed out the likelihood for significant variation of supershell properties in galaxies of different Hubble type. Kamphuis (1993) analyzed the giant spiral M101, drawing a tentative connection between high-velocity clouds (HVCs) and the supershell phenomenon. Most recently, Staveley-Smith et al. (1997) took advantage of the ATNF in order to survey the SMC at unsurpassed spatial resolution and found more than 500 expanding shells. While the aforementioned studies were suc-

*Send offprint requests to*: David A. Thilker (dthilker@nmsu.edu)
⋆ Visiting observer, Kitt Peak National Observatory

cessful in showing that HI shells are common, they were limited by having to rely on *visual* identification of expanding structures in a spectral line datacube. Such a procedure is challenging because it requires the eye to recognize complex, rapidly changing, and filamentary patterns distributed throughout a number of datacube channel-maps. In practice, this requirement led to surveys focused on the most-easily recognizable kinematic signature - an expanding, spherical bubble. Realistic analysis of supershells in a large sample of galaxies was precluded by the lack of a computer-based shell detection method.

We have created an automated object recognition package capable of finding user-specified, 3-dimensional patterns in a datacube. This software tool enables unbiased detection and characterization of supershells in spectral line datacubes, provided our modeling of shell evolution is accurate. Our package: (1) determines the *approximate* predicted observable appearance for template supershells of any size and expansion velocity, (2) employs a robust cross-correlation procedure to identify datacube regions matching these characteristic patterns, and (3) computes basic properties for all observed supershells, based on the "best-fit" supershell model of each detection. Several factors are crucial to the effectiveness of our software. In particular, we designed the code to allow for models not limited by spherical symmetry, incorporate projection effects due to inclination, and search for supershell signatures convolved with the instrumental beam. The automated package will allow us to compile a data-quality limited shell catalog for any nearby system having suitable observations. Eventually we hope to rigorously test competing supershell models.

The idea of an automated detection algorithm for supershells is not something new. Hu (1981) successfully developed a method for easily identifying the filamentary signature of an expanding supershell in the Galactic HI survey of Heiles & Habing (1974). The technique worked by filtering HI data in velocity space, but was not based on searching for the predicted appearance of a supershell model. Instead, Hu used a completely analytic, tunable filter which transformed datacubes into images with shell-like features artificially enhanced over slowly-varying "background" gas. Unfortunately, Hu's method is likely inapplicable to nearby spirals, in which surface brightness sensitivity and spatial resolution greatly hampers shell detection.

We intend to apply our object recognition software for the systematic analysis of 21 galaxies for which high-resolution HI data are available. We will address several unresolved questions concerning gaseous supershells. For instance, what fraction of shells cannot be powered by massive stars? What factors regulate the evolution of a supershell? Oey (1996) compared the observed size and expansion velocity of six young LMC superbubbles with model predictions calibrated according to the stellar content of each structure. For half of her sample, Oey noted significant kinematic discrepancy between model and data, suggesting the importance of stochastic events (individual SNe) in the evolution of shells powered by a small number of OB stars. In such cases it appears that a single supernova may substantially boost the instantaneous expansion velocity of its associated shell. This concern is not a limitation to our study because the HI shells we detect usually involve more SNe and are always much larger than the ionized bubbles observed by Oey. Do superbubble characteristics vary predictably as a function of ambient environment or position within a spiral disk? Furthermore, what is the rate of mass and energy transfer between disk and halo via the "chimney" structures of Norman & Ikeuchi (1989)? We hope that systematic, repeatable analysis of the supershell population in a large sample of galaxies will answer these (and other) open questions.

In Sect. 2 we describe the automated object recognition package, specifying how we have initially elected to compute the predicted appearance of different supershell types and the way in which we characterize detections. The shell modeling scheme described in Sect. 2 provides only first-order agreement with more realistic numerical models. It will be replaced with a more robust treatment in future papers. We discuss the observed supershell population for NGC 2403 in Sect. 3, including a global analysis of shell properties and detailed review of catalog completeness issues. A few shells are featured for demonstration. In Sect. 4 we summarize our conclusions and relate future plans for the automated package.

This paper is the first in a series. We expect the preliminary HI shell catalog presented here to evolve somewhat as our package is refined.

## 2. Automated object recognition method

We first outline our general procedure and then discuss individual steps in greater detail below.

### *2.1. Overall procedure*

Our automated detection algorithm is based on identifying the most significant, compact peaks in the cross-correlation of a high-resolution spectral line datacube with a grid of "shell model datacubes". The basic steps are given below.

1. We employ an analytic model for the evolution of a supershell powered by constant mechanical luminosity to derive the approximate physical structure of an expanding shell having specified in-plane radius and expansion velocity. We derive the density and expansion velocity of gas in the region occupied by the shell. Shell evolution is assumed to take place within a multi-layer, plane-stratified gaseous disk. As explained below, this type of ambient disk model was viewed as the first logical step beyond uniform environment shell evolution, but still less in-depth than adopting a smoothly varying density profile.

2. The physical model from Step 1 is projected into an "observable" datacube representation. This model datacube consists of images of predicted HI emission brightness in specified velocity intervals. We account for spatial orientation of the shell-hosting galaxy in addition to the instrumental resolution.

3. Both the user-supplied datacube and our model datacube are Fourier transformed in three dimensions. Next, the complex product is formed of the transformed data with the complex conjugate of the transformed model. Subsequently, this result is inverse Fourier transformed to obtain the correlation signal.

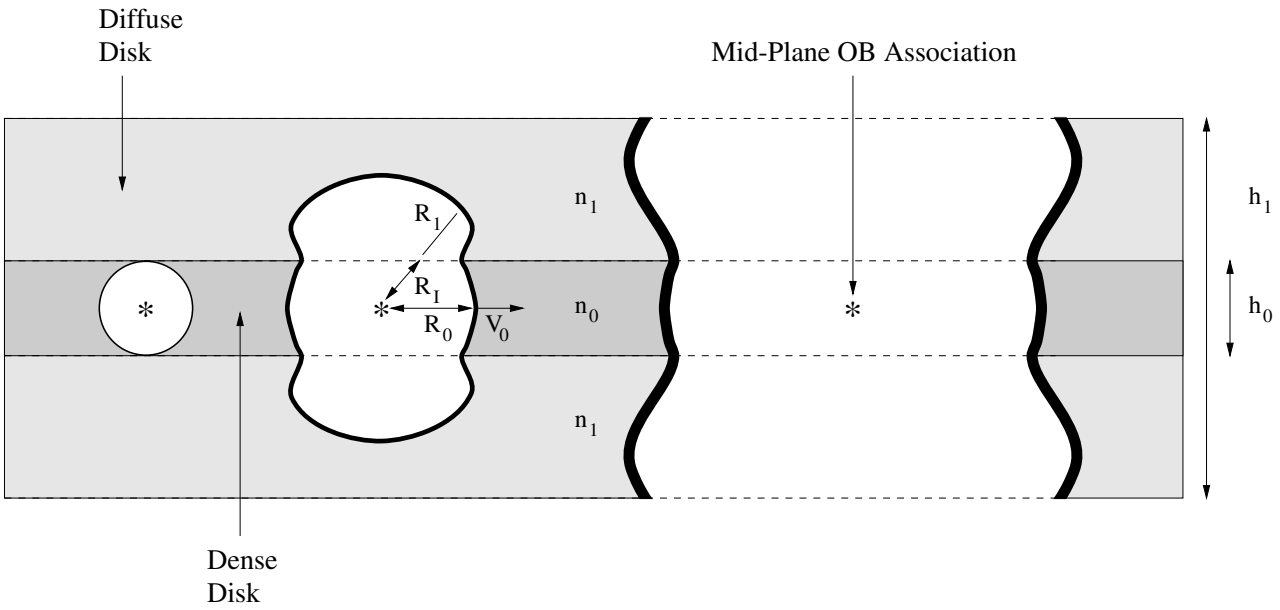


**Fig. 1.** Edge-on view of the neutral, plane-stratified ambient disk assumed in our models and a collection of typical HI shells. Notice the diffuse neutral gas disk which completely envelopes a thin, dense, central layer. Beyond these neutral regions we assumed a completely ionized environment in pressure equilibrium with the diffuse HI layer. Because ionized gas extends infinitely away from the disk and does not contribute to our neutral shell signatures, it is not depicted in this figure. Three characteristic varieties of supershell have been depicted: on the left, a small spherical bubble; in the center, a medium-sized "mushroom-top" shell; and, on the right, a chimney or "hourglass" break-out structure. We indicate how the in-plane radius ($R_0$), expansion velocity ($V_0$), $R_1$, and $R_I$ are defined for the central shell.

Local maxima within the correlated cube indicate regions which are well-matched by the projected model shell.

4. Since we are only interested in compact peaks within the correlated cube, we apply a high-pass filter to individual planes of this product. This step provides enhanced contrast of the peaks, as well as a local background subtraction.

5. All point-like structure in the filtered, correlated cube is extracted. These sources are tabulated down to a specified multiple of the rms fluctuation level.

6. Multiple detections of the same peak within adjoining planes of the filtered, correlated cube are eliminated. Only the most significant within each group is retained.

7. Steps 1 through 6 are repeated for a complete grid of trial supershell radii and expansion velocities.

8. Correlation peaks due to a single observed shell structure are typically found over a range of model radii and expansion velocities where that structure is approximately fit. Redundant detections of this sort are eliminated and only the most significant of each set is retained. Our shell catalog is composed of these best-match detections.

### *2.2. Shell expansion model*

The shell expansion model adopted in our analysis is the adiabatic similarity solution for a constant mechanical luminosity derived by Weaver et al. (1977). See their Eq. (21). Following McCray & Kafatos (1987), we substitute the time averaged mechanical energy input from supernovae for the stellar wind luminosity originally assumed by Weaver. This should be appropriate at times when supernovae dominate stellar winds as the source of mechanical energy for an OB association. The mechanical luminosity due to discrete supernovae is approximated as a constant, continuous source. This assumption is not valid in general, but for coeval associations having an IMF given by $dN/d(logM) \sim M^{-1.6}$, McCray & Kafatos show that flat energy input is a good approximation if the cluster is younger than 50 Myr old. Most of the model shells computed for our analysis are younger than this limit. Shull & Saken (1995) demonstrate that the assumption of constant energy input is quite poor for noncoeval star formation. Nevertheless, for simplicity, we assume truly coeval associations and a constant mechanical luminosity in our current modeling. The influence of these assumptions plays only a small role in locating expanding shells, although it may well be of importance during subsequent interpretation of results. Eqs. (1) and (2) present the adopted expansion model in terms of shell radius and expansion velocity as a function of time:

$$\mathrm{R} = 97 \left(\frac{\mathrm{N_* E_{51}}}{\mathrm{n}}\right)^{1/5} \mathrm{t_7}^{3/5} \ \mathrm{pc}, \tag{1}$$

$$\mathrm{V} = 5.7 \left(\frac{\mathrm{N_* E_{51}}}{\mathrm{n}}\right)^{1/5} \mathrm{t_7}^{-2/5} \ \mathrm{km\ s^{-1}}. \tag{2}$$

In these expressions, $t_7$ is the age of the shell in units of 10 Myr, $N_*$ is the number of stars formed with mass $> 7\ M_\odot$, $E_{51}$ is the assumed energy per supernova (expressed in units of $10^{51}$ erg), and $n$ is the density of the ambient gas (atoms cm$^{-3}$).

The predictions of Weaver (1977) and McCray & Kafatos (1987) are strictly valid only for shells growing in a uniform environment. Because our intent was to model structures often larger than the disk scale height for HI we clearly needed to adopt a somewhat modified solution in which large bubbles preferentially expand out of the plane. Eqs. (1) and (2) were used to derive approximate shell structure for evolution in a five-layer, plane-stratified ambient medium. We describe our exact technique in the following paragraphs, but first introduce a few parameters related to the disk model.

Fig. 1 presents a schematic edge-on view of various shells within our simplified galaxy plane. This adopted ambient medium is meant to approximate the true vertical structure of HI in a spiral galaxy by including a thin, dense disk with density, $n = n_0$, and full thickness, $h = h_0$, enveloped by a diffuse disk of lower density, $n = n_1$ and full thickness, $h = h_1$. Beyond this HI disk we assume the presence of an ionized component with density $n = n_1/2$, forcing pressure equilibrium with the diffuse neutral disk. This ionized environment is analogous to the Reynolds layer in the Galaxy (Reynolds 1991), although for simplicity our ionized layer extends infinitely away from the plane. Adopting the nominal ratios of $n_0/n_1 = 3.3$ and $h_1/h_0 = 4$ provides a reasonable step-wise approximation to an exponential distribution in $|z|$ with central density $n_0$ and exponential scale height $h_0$. In reality, the distribution of ambient density is undoubtedly more complex. Below we show below that our results agree well with hydrodynamic simulations employing an exponential vertical density distribution, which is probably more realistic.

We chose to use the analytic similarity model with our empirical extension to a plane-stratified medium because it allows substantial flexibility with only a modest investment in computation, while retaining the essential properties of supershell expansion. Although a number of authors have presented semi-analytic models of shell evolution in non-uniform ambient environments (eg. Ferrière et al. 1991, Koo & McKee 1990, Mac Low et al. 1989), no suitable fully-analytic model has yet been published for supershell evolution in a realistic density distribution. In the future we will calculate a complete grid of hydrodynamic simulations as a starting point, but this level of sophistication was beyond the scope of our initial investigation.

Within the assumed ambient disk, we solve for both the density and expansion velocity of gas about a mid-plane shell origin. This origin pinpoints the location of a progenitor OB association, the only source of mechanical luminosity in our model. Clearly not all supershells will form centered in the galactic plane. However, we currently neglect the fact that such highly asymmetric supershells are likely to develop. Any other approach would be computationally prohibitive and further compromise the accuracy of our shell modeling code. Cylindrical symmetry is assumed in our analysis. Consequently, shear due to differential galactic rotation is ignored (see Sect. 2.3).

All model supershells are parameterized in terms of $R_0$, their in-disk radius, and $V_0$, their in-disk expansion velocity. By choosing $R_0$ and $V_0$, we are able to determine $t_7$ and $(N_* E_{51}/n_0)$, giving us both the age of the parameterized shell and a measure

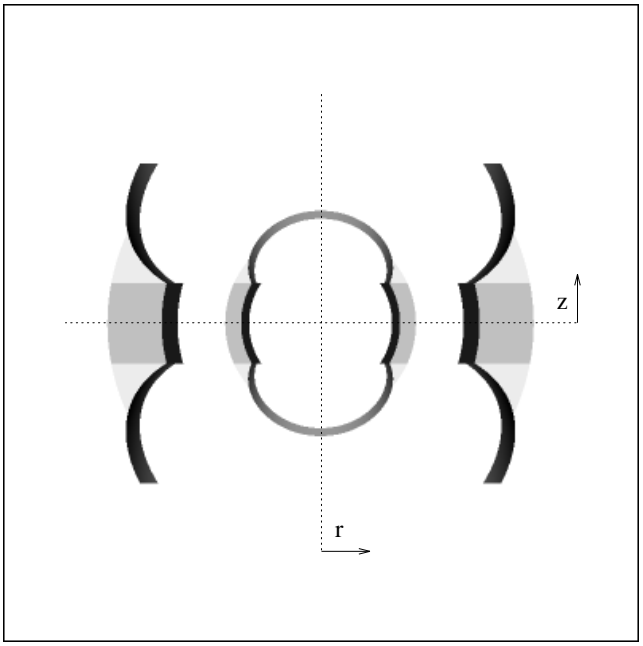


**Fig. 2.** Edge-on view of the spatial models generated by our code for $R_0 = 100$ pc and $R_0 = 200$ pc with $(h_0, h_1) = (100, 400)$ pc and $(n_0, n_1) = (1.0, 0.3)$ cm$^{-3}$. In this cross-cut, we display the density of HI with a linear intensity scale and center both structures on a common origin. The swept-up shell, evacuated cavity, dense disk, and diffuse disk are all evident. Density ranges from 0.3 cm$^{-3}$ in the diffuse disk, through 1.0 cm$^{-3}$ in the dense disk, and up to $\sim$ 3 cm$^{-3}$ within each shell. The cavity was assigned a neutral density of zero. The total image size is 800 pc.

of richness for the shell's progenitor stellar population. Note that the implied value of $N_*$ for any particular bubble depends on $n_0$, the mid-plane gas density before shell formation. Since $n_0$ will vary with location in a shell hosting galaxy, we must derive $N_*$ on a shell-by-shell basis once an estimate of the local gas density is known. This issue is discussed further in Sect. 2.6.

Our modeling code determines the approximate distance from the mid-plane origin to the outer shell wall along all lines-of-sight. Everywhere that the shell remains contained within the dense disk, it has radius and expansion velocity which follow immediately from Eqs. (1) and (2).

For pixels within the diffuse disk, the process of determining a shell radius and velocity is complicated by the changing ambient density encountered at a radius $R_I$ along such radii. We assume that a velocity discontinuity of magnitude $(n_0/n_1)^\alpha$ is experienced at the density interface giving,

$$R_1 = R_I + \left(\frac{n_0}{n_1}\right)^\alpha (R_0 - R_I), \tag{3}$$

$$V_1 = 5.7 \left(\frac{n_0}{n_1}\right)^\alpha \left(\frac{N_* E_{51}}{n_0}\right)^{1/5} t_7{}^{-2/5} \text{ km s}^{-1}. \tag{4}$$

A value of the density index, $\alpha = 0.5$, was chosen based on the jump condition for conserving ram pressure across a density interface ($n_0 V_0{}^2 = n_1 V_1{}^2$) and provides good agreement

of the calculated shell shape with numerical models of Mac Low & McCray (1988) for a corresponding exponential vertical density distribution. In the case of supershells expanding within the diffuse disk phase, the maximum out-of-plane shell radius is typically a factor of 1.3–1.6 greater than $R_0$. Fig. 2 depicts density cross-cuts through the center of two shells with in-plane radii of 100 and 200 pc. For these model calculations, we assumed ($h_0$, $h_1$) = (100, 400) pc and ($n_0$, $n_1$) = (1.0, 0.3) cm$^{-3}$.

Having computed the approximate shell radius in all directions about the origin and assuming that the shell has a thickness of 0.1 $R_0$, we can determine whether any given pixel is part of the shell, the undisturbed ambient medium, or lies within the shell cavity. Those pixels found to be within the evacuated shell cavity are assigned a neutral density of zero. Undisturbed ambient-gas pixels receive a value of either $n_0$ or $n_1$, depending on whether they belong to the dense or diffuse neutral disk. All pixels with $|z| \geq h_1$ were assumed to be fully ionized and do not contribute to our models. For pixels belonging to the shell, we self-consistently determine $n_H$ by integrating all of the ambient gas swept up along a line-of-sight from the shell origin to the outer shell wall and distributing this uniformly in a layer between R and R $-$ 0.1 $R_0$. For the choices of $R_0$ included in our survey, the mean shell density was typically $\sim$3 $n_0$. 3-D numerical hydrodynamic shell simulations yield similar density contrasts (Mashchenko, private communication).

During channel-map projection, we include a small spherical region of undisturbed ambient gas as part of the basic shell signature. This volume was truncated in radius when the mass of ambient HI equaled 1/3 of all swept-up HI. Our motivation for taking along ambient gas is that it should reduce the likelihood of spurious detections substantially offset from channels filled with emission from the shell hosting galaxy.

Every spatial pixel must be associated with an assumed velocity dispersion value before we proceed with projection of the model as described in Sect. 2.3. We allow pixels belonging to the shell, dense disk, and diffuse disk to have intrinsically different dispersions.

A potential shortcoming of our modeling approach is the implicit assumption that all radial paths will evolve independently of one another. The underlying physical assumption is that there is negligible venting of the pressure driving superbubble expansion. This becomes an increasingly poor assumption as the shell extends beyond $|z| = h_1$. However, an ionized "Reynolds" layer, if present, could prevent venting until much later in the structure's evolution. As noted above, our models do incorporate such a layer, modeling the dynamical evolution of the neutral shell as if its ionized cap effectively contains the superbubble cavity pressure.

Fig. 1 illustrates the three general "families" of supershell structure approximated by our model. For the lowest values of $R_0$, the shell remains spherical in shape. Intermediate values of $R_0$ yield "mushroom-like" structures. Finally, for the largest values of in-disk radius, the model supershell breaks out of the ambient disk, assuming a "chimney" form, similar in appearance to an hourglass. For all three shell morphologies, we can generate expanding and stalled models. Stalled models are derived by assuming an arbitrarily small value for $V_0$.

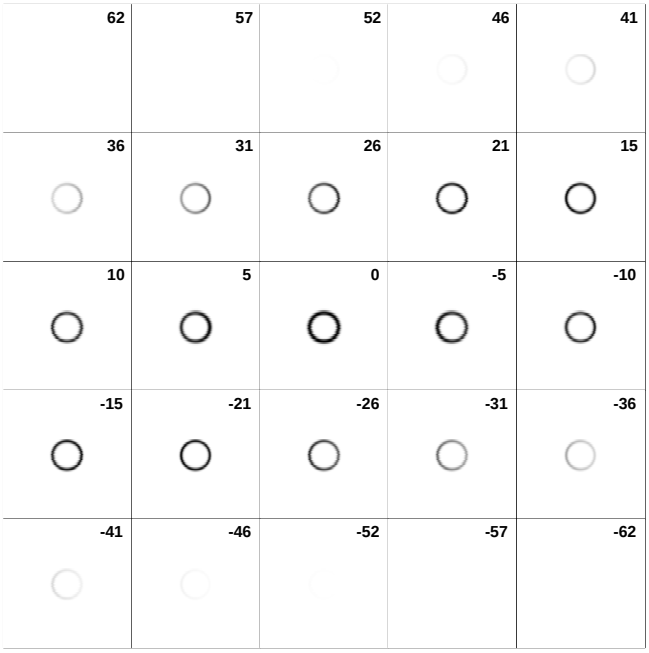


**Fig. 3.** Channel-map array illustrating the "observable" datacube signature of a model shell with ($R_0$, $V_0$) = (200 pc, 20 km s$^{-1}$). This figure was generated for the case of a face-on spiral disk, having $i = 0°$. Heliocentric velocity with respect to the central channel is indicated in each frame and measured in km s$^{-1}$. The galaxy major axis is oriented horizontally.

### 2.3. Channel-map projection

We next project the physical structure of the parameterized shell into channel-map space, deriving an "observable" datacube signature for the appropriate orientation of the host galaxy. Correcting for galaxy inclination and orientation is a unique and critical feature of our search algorithm. The following steps are involved in the projection:

1. For each pixel in the 3-D volume defined by our physical model, designated the (X,Y,Z) space, we determine two projected spatial coordinates (L,M) and the component of radial expansion velocity directed along the line-of-sight to the observer, $V_{los}$, for the appropriate inclination and orientation of the host galaxy.

2. Next we determine $V_{corr}$, a first-order correction for the change of systemic velocity across a shell due to galactic rotation. This is accomplished by applying an average velocity "slope" (measured in km s$^{-1}$ kpc$^{-1}$) along the direction of the major axis of the galaxy. $V_{corr}$ is computed from this simplified parameterization of galactic rotation and each pixel in a shell is assigned a corrected velocity, $V = V_{los} + V_{corr}$. Note that $V_{corr}$ varies within a single shell, taking on a new value for each pixel in a different projected location. Since only a single shell model is correlated with the entire galactic disk at any given

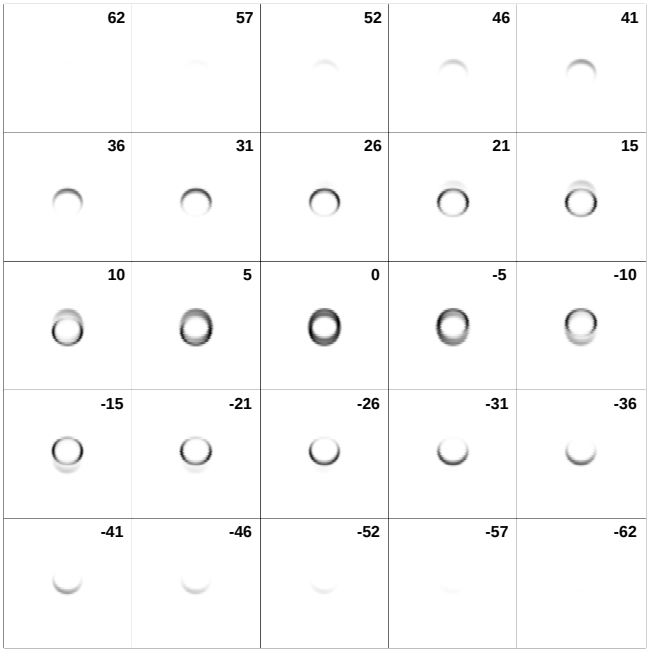


**Fig. 4.** As for Fig. 3, except assuming $i$ = 30°.

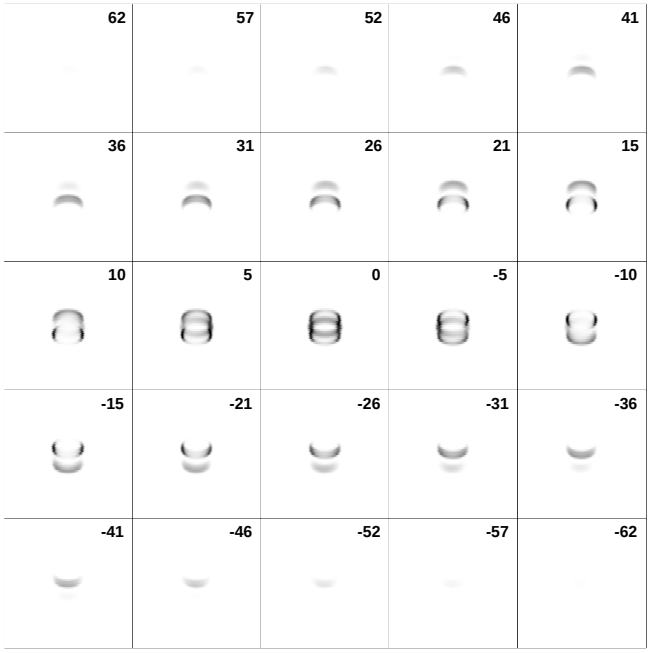


**Fig. 5.** As for Fig. 3, except assuming $i$ = 60°.

time we cannot include refinements which depend on position within the disk, such as galactic shear (see Silich et al. 1996a, Tenorio-Tagle & Palous 1987) or a realistic disk-rotation model.

3. The values of neutral gas density for each model pixel are accumulated into a binned (L,M,V) representation which has the same spatial-velocity grid as the datacube being analyzed. The distance to the host galaxy is incorporated at this stage. Densities are distributed over velocity according to the velocity dispersion and central velocity of each model pixel. The inherent assumption in this step is that the HI emission is optically thin. Although it would be possible to carry out a calculation of HI intensity using appropriate radiative transfer, this would only be relevant for one particular choice of density and could not easily be scaled.

4. The binned (L,M,V) cube is convolved with an appropriate point spread function to match the instrumental resolution of the user-supplied datacube.

5. The output (L,M,V) cube is normalized to have unit peak intensity.

To illustrate the remarkable dependence of the predicted supershell appearance on galaxy inclination we present the "channel-map arrays" shown in Figs. 3–5. Each array shows the predicted datacube signature of a parameterized shell having $R_0$ = 200 pc and $V_0$ = 20 km s$^{-1}$. For this demonstration we have assumed unrealistically good spatial resolution, especially considering that most of our sample galaxies are located beyond 3 Mpc. The three figures correspond to galaxy inclinations of $i = 0°, 30°,$ and 60°. The assumed ambient disk parameters are held fixed at ($h_0$, $h_1$) = (100, 400) pc and ($n_0$, $n_1$) = (1.0, 0.3) cm$^{-3}$. In each array, we show the central 25 channel-maps from the model datacube. Line-of-sight velocities (with respect to the central velocity of the shell) for each channel are indicated. The supershell datacube signatures are computed for an instrumental PSF of 35 pc FWHM spatially and a 5 km s$^{-1}$ top-hat in velocity. The maps in Figs. 3–5 should not be directly compared with later figures illustrating data for NGC 2403 because our actual cubes have angular resolution degraded by a factor of four with respect to this idealistic presentation.

For a face-on galaxy each channel-map is characterized by a simple pattern having nearly-circular symmetry. Any departures from circular symmetry are due to the ambient medium's "tilted" rest-velocity floor. Contributing most of the emission in our zero-inclination signature is a dense inner ring, prominent throughout the central channels. The doughnut-like appearance of each channel-map in Fig. 3 arises due to the chimney structure for a shell with $R_0$ = 200 pc. The two high velocity caps extend beyond the diffuse disk and are assumed to be fully ionized. Refer to Fig. 2 for a density cross-cut of this shell.

Fig. 4 indicates how the same shell looks when observed at $i$ = 30°. The circular symmetry of the face-on case has vanished. Instead, the observable datacube signature is characterized by reflection symmetry about the major axis. All prominent emission is found in the form of arclets arising in the edge-brightened chimney walls.

The $i$ = 60° case is illustrated in Fig. 5. Notice how the innermost regions of the central velocity channel are nearly filled with emission from the ambient medium just outside the HI shell. Indeed, the "HI hole" morphology used as a search criterion in most previous supershell searches rapidly vanishes as inclination is increased. The observable signature of a highly inclined supershell does not have much of a local minimum at

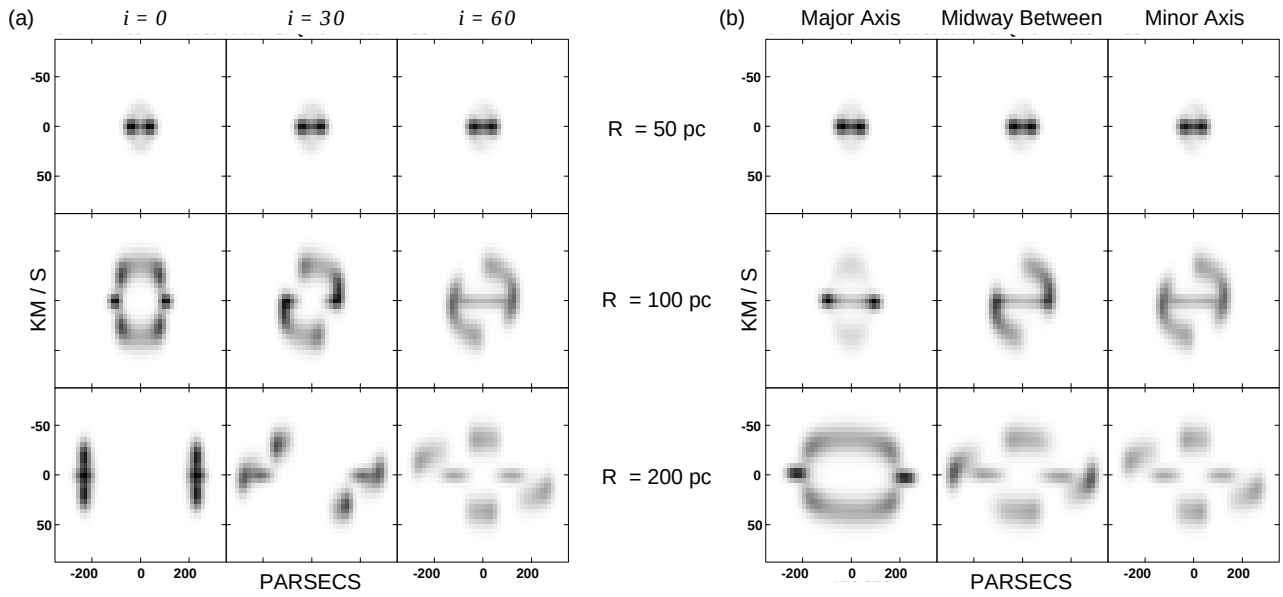


**Fig. 6a and b.** Synthetic position-velocity diagrams for shell structures with in-plane radii of 50, 100, and 200 pc. Each shell was assigned an expansion velocity of 20 km $s^{-1}$. Panel **a** illustrates the dependence of minor axis P-V morphology on galaxy inclination. Panel **b** shows how the choice of cross-cut orientation (with respect to a galaxy's line-of-nodes) can dramatically influence the appearance of P-V diagrams. In panel **b**, the P-V diagrams are shown for i = 60°.

its central position, neither on the sky nor in velocity. Fig. 5 clearly demonstrates the importance of accounting for projection effects due to galaxy inclination whenever attempting to locate and characterize expanding gaseous shells.

Position-velocity (P-V) diagrams have also been used to look for expanding HI shells (e.g. Brinks & Bajaja 1986). The effects of projection due to inclination and orientation also dramatically influence P-V diagram morphology. Simple "velocity splitting", often demanded as evidence of supershell expansion, is only a first-order description of the predicted P-V structure. All of the following factors are important when predicting or interpreting an observed P-V diagram: (1) the orientation of the cross-cut with respect to the host galaxy's line-of-nodes, (2) the size and expansion velocity of a supershell, and (3) the galaxy inclination. These points are illustrated in Fig. 6.

In Fig. 6a we show minor axis P-V cross-cuts for shells with in-plane radii, $R_0$ = 50, 100, and 200 pc; and having host galaxy inclinations, $i = 0°, 30°$, and 60°. All shells were assigned an in-plane expansion velocity, $V_0$, of 20 km $s^{-1}$. Note only the smallest shells have P-V diagrams which are independent of inclination. Larger non-spherical shells show increasingly distorted structure at substantial inclinations.

In Fig. 6b we consider the same three shell types as before but hold the inclination fixed at $i = 60°$, and display the cross-cut orientations $\Delta\phi = 0°, 45°$, and 90° with respect to the galaxy major axis. Note how the P-V structure changes dramatically with cross-cut orientation for radii greater than about 100 pc. It is also striking that the magnitude of velocity splitting is both dependent on cross-cut orientation, and much faster ($\sim$40 km $s^{-1}$) than the in-plane expansion velocity, $V_0$ = 20 km $s^{-1}$. These variations highlight another virtue of fitting the data to physical models having known parameters. Every such model is associated with a well-defined mass and kinetic energy. In contrast, shell kinetic energy estimates based on expansion velocities derived from velocity splitting and a total in-plane mass can easily be in error by over an order of magnitude.

### *2.4. Correlation and filtering of the data*

Next we compute the filtered cross-correlation of an observed datacube with the model datacube. This is most efficiently done using a Fast Fourier Transform (FFT). The correlation and filtering is accomplished by: (1) individually calculating the 3-dimensional FFT of both the input data and the model cube, (2) forming the complex product of the FFT'ed data with the complex conjugate of the FFT'ed model, (3) multiplying the complex product with a filtering function, and (4) taking the inverse 3-D FFT of this tapered complex product.

Compact peaks in the correlated datacube are probable shell locations, while the intensity of each peak is proportional to the detected shell mass.

In order to illustrate our technique, Figs. 7a and 7b show a channel-map subsection of the galaxy NGC 2403 before and after the correlation procedure. We selected a channel at the rest velocity of a prominent supershell in order to make the demonstration most effective, although the automated procedure works equally well for expanding shells which are not as visually distinct. The central peak in Fig. 7b is the result of correlation with a model shell having $R_0$ = 300 pc and $V_0$ = 10 km $s^{-1}$. The position of this shell has been indicated with a cross on both images. The two axes of the cross specify the projected in-

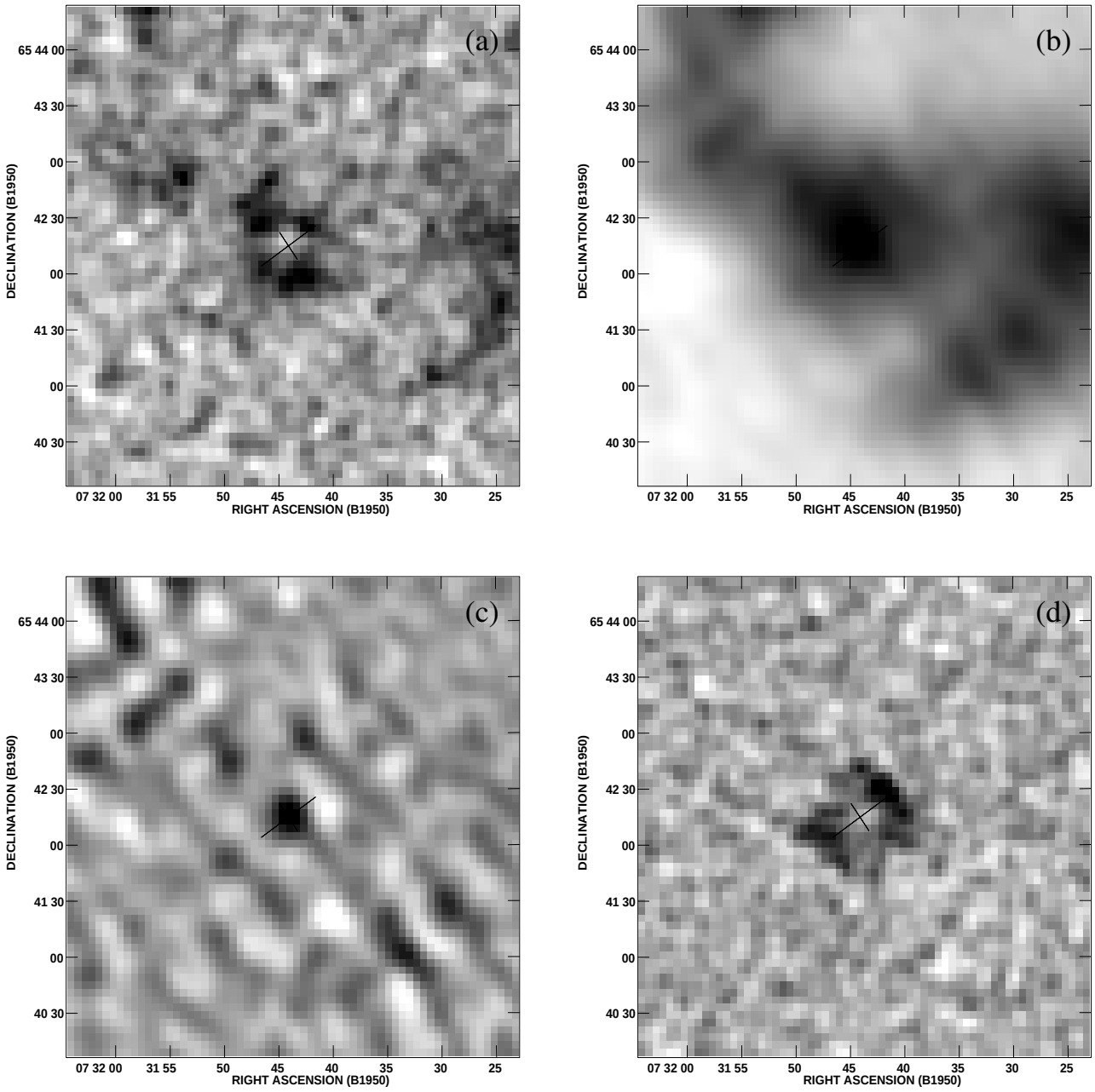


**Fig. 7a–d.** These 4 images illustrate the effectiveness of the cross-correlation, high-pass filtering algorithm in our automated object recognition package. Panel **a** shows a channel-map subsection centered on a shell found as part of our NGC 2403 survey. The supershell has ($R_0$, $V_0$) = (300 pc, 10 km $s^{-1}$). The position of this shell is indicated using a cross with dimensions scaled to the projected size of its major and minor axes. Panel **b** shows the result of datacube cross-correlation, using a model cube matched to the shell's parameters. Note the strong correlation peak at the position of the shell in question. After high-pass filtering, we have the result depicted in panel **c**. A few other supershells exist within the region depicted in this figure, but are centered in neighboring channels or "best-fit" by a different ($R_0$,$V_0$) model. Consequently, they are not evident in panels **a–c**. Panel **d** presents a channel-map of the best-fit model associated with the shell centered in panel **a**. We have added noise to the model, enabling fair comparison with panel **a**.

plane dimensions of the HI cavity. Note the excellent agreement between the apparent center of the shell structure (in Fig. 7a) and the position (in Fig. 7b) of the correlation peak. Other shells also exist within this image section, but have not been marked here. They are either centered in adjoining channels or are better matched by different model parameters.

We experimented with various high-pass filters applied in the Fourier plane to isolate compact correlation peaks from a slowly varying background. The most successful form for suppressing the background while minimizing side-lobe ringing was:

$$W = 1 - 0.5\, e^{\ln(0.01)(S-B)/B} \quad \text{for } S > B, \tag{5}$$

$$W = 0 + 0.5\, e^{\ln(0.01)(B-S)/B} \quad \text{for } S \leq B, \tag{6}$$

where W is the multiplicative weight given to a Fourier component having spatial frequency, S, and B is the inflection point of the filter function, as illustrated in Fig. 8. Values of B corresponding to $\sim$6 times the synthesized beam size were empirically found to optimize signal to noise. Fig. 7c illustrates the correlated channel-map of Fig. 7b after completion of high pass filtering. The contrast of compact, point-like maxima in the image plane is considerably enhanced. For comparison with data, panel (d) shows a channel-map of the best-fit model associated with the shell featured in panel (a). Noise has been added to our model to permit fair assessment of the match between observations and model. We note that our pattern recognition package uses all the information contained in a 3D volume to determine the quality of a match, not just one 2D slice.

### *2.5. Source extraction & normalization*

In the absence of a truly three-dimensional algorithm for the extraction of compact peaks in the correlated, high-pass filtered datacubes, we made use of an iterative procedure within the AIPS software package to obtain a similar result. Our extraction method employs the Search-and-Destroy (SAD) task to produce an output table listing all the peak detections above a specified significance level (typically $4\sigma$) within each velocity channel of a processed cube. Local maxima in each channel are fit by elliptical Gaussian components and are then subtracted from the data. The threshold level for peak extraction in a channel-map begins with the maximum observed intensity and decreases in each subsequent iteration using steps of one-half the rms fluctuation level. In order to exclude edge effects, no peaks within 32 spatial pixels or 2 velocity channels from the edge of the datacube are extracted. One table of "potential detections" is generated in this way for each model shell type included in our parameter grid.

Next, outside of the AIPS environment, we sort through the list of potential shell detections (correlation peaks) associated with each parameterized signature and exclude all redundant or suspect entries (typically $\sim$ 90%) for one of three well-defined reasons: (1) the entry does not meet a specified significance criteria ($T_{cat}$, typically $6\sigma$), (2) the entry is not "confirmed" by having at least several "overlapping" detections in adjacent channels, or (3) the entry is itself only the "confirmation" of some other, more significant entry. This step primarily eliminates multiple 2-D entries associated with the same 3-D correlation peak, but also removes spurious "noise-like" detections not corroborated with neighboring detections in adjacent velocity channels. "Overlap" is determined from comparison of the candidate shell positions with the dimensions of their elliptical Gaussian components.

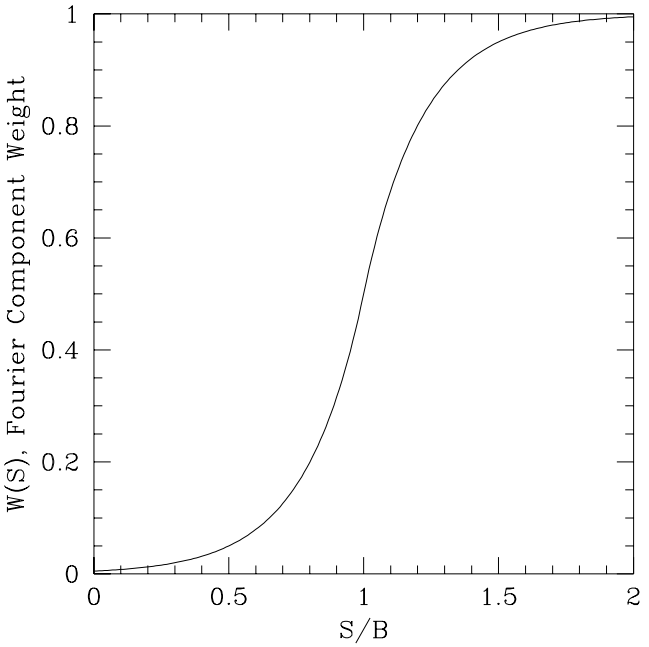


**Fig. 8.** W, the high-pass filtering function (used to enhance the contrast of compact cross-correlation peaks) is plotted as a function of S/B.

The high-pass filter function described in Sect. 2.4 has a large influence on the tabulated amplitude of each correlation peak. The magnitude of this effect changes on a kernel to kernel basis and must be removed in some manner before evaluation of detection significance and various other shell properties. Renormalization of correlation peak amplitudes is determined by calculating the filtered auto-correlation of each model shell and tabulating its peak value. In this way we calibrate the shell mass returned by our procedure via the detection of model shells with known properties.

The next step in the production of a shell catalog is to eliminate multiple detections of the same observed structure over a range of ($R_0$,$V_0$) . In practise, coincident correlation peaks are often detected over a range of about 2–3 grid samples (as defined in Table 5) in both variables. Choosing only the single, most significant, coincident detection corresponds to a parameter space "fitting" of each structure. Since we are not actually carrying out a minimization of fit-residuals with respect to each model, there could, in principle, be some ambiguity in choosing the "most significant" detection.

We empirically determined the assignment of detection "significance" with a set of simulations. Model shell signatures with

a range of specified ($R_0$,$V_0$) and a range of HI masses were inserted into an HI datacube of the galaxy NGC 2403. These artificial shell signatures were then extracted automatically together with the ones present in the data using the processing steps outlined above. We experimented with various significance ranking schemes, including optimization of signal-to-noise and purely signal (detected shell mass). In order to recover the correct ($R_0$,$V_0$) for inserted shells, it was necessary to maximize a quantity proportional to the square of cross-correlated signal (properly normalized for each kernel type). Maximizing the signal-to-noise ratio resulted in a systematic bias of the detections to lower expansion velocity. For injected shells in the same mass range as those typically encountered in the actual data, the precision of parameter recovery was better than one grid sample in each of ($R_0$,$V_0$) corresponding to 1/3 of the instrumental beam FWHM in radius and 30–40% in velocity. It seems likely that our precision in $V_0$ could be improved by sampling parameter space with a smaller grid spacing, although this is computationally prohibitive at the moment.

Having established the appropriate criterion for assessing detection significance, all of the coincident, but comparatively insignificant, shell detections were discarded from the catalog.

### *2.6. Cataloged shell characteristics*

The first several variables included in our catalog description of each shell are rather straightforward. We provide the equatorial coordinates and systemic velocity of the shell center, along with the best-matched ($R_0$,$V_0$) parameters. In addition, the galactocentric radius, inferred shell age, and signal-to-noise ratio of the detection are simple to tabulate.

Shell age, $t_7$ (in units of 10 Myr), is implied directly by the values of $R_0$ and $V_0$ from Eqs. (1) and (2), irrespective of the ambient density, via:

$$t_7 = \left(\frac{5.7 \text{ km s}^{-1}}{V_0}\right)\left(\frac{R_0}{97 \text{ pc}}\right). \quad (7)$$

It is important to note that our method of computing $t_7$ is *not* equivalent to simply deriving the quantity from visual estimates of projected shell radius and line-of-sight "velocity splitting". Values for $t_7$ calculated using Eq. (7) are directly related to the adopted shell expansion model (of Sect. 2.2) since we use the best-fit *in-plane* radius and velocity parameters. Our method explicitly accounts for projection effects due to inclination.

Of the remaining catalog variables, we begin by computing $(M_{HI})_{obs}$, the observed HI mass consistent with our velocity-projected supershell signature. This quantity follows directly from the correlated signal strength of each shell detection, $S_c$, in units of Jy pixel$^{-1}$. The observed HI mass is:

$$(M_{HI})_{obs} = 2.36 \text{ x } 10^5 \left(\frac{D}{\text{Mpc}}\right)^2 \left(\frac{\Delta v_{ch}}{\text{km s}^{-1}}\right) \eta \, S_c \, M_\odot, \quad (8)$$

where D is the assumed galaxy distance, $\Delta v_{ch}$ is the datacube channel spacing, and $\eta$ is the fraction of a kernel's total HI mass accounted for by shell structure (always $\sim$0.75, as indicated in Sect. 2.2).

Knowing $(M_{HI})_{obs}$ for a given shell implies an effective midplane ambient density by a simple scaling of the HI mass of the corresponding model shell, $n_{eff} = n_0 \, (M_{HI})_{obs}/(M_{HI})_{model}$. Although obviously not true, we implicitly assume every shell is complete. We discuss how the accuracy of this assumption can be tested at the end of this section. Substituting $n_{eff}$ for $n_0$ allows calculation of $N_*$, from Eqs. (1) and (2).

$$N_* = \frac{n_{eff}}{E_{51}} \left(\frac{R_0}{97 \text{ pc}}\right)^2 \left(\frac{V_0}{5.7 \text{ km s}^{-1}}\right)^3 \quad (9)$$

The kinetic energy associated with each neutral shell, $(E_k)_{obs}$ is determined via linear scaling by mass of the kinetic energy associated with the appropriate model, $(E_k)_{obs} = (E_k)_{model} \, (M_{HI})_{obs}/(M_{HI})_{model}$. $(E_k)_{model}$ is evaluated by a summation of the product of mass and squared expansion velocity associated with every pixel in the physical shell model. Density values are scaled by a factor of 1.4 to account for the presence of helium.

It is possible to directly estimate the mean ambient density, $<n(HI)>$, in the environment of each detected shell structure. This is accomplished by measuring the average column density, $<N(HI)>$, within a projected radius of 1.25 $R_0$ in an image of integrated HI emission and then dividing $<N(HI)>$ by the effective pathlength,

$$d = 3.086 \text{ x } 10^{18} \frac{h_0}{\cos i} \left(1 + \frac{n_1}{n_0}\left(\frac{h_1}{h_0} - 1\right)\right) \text{ cm}, \quad (10)$$

defined in terms of the model disk parameters, ($h_0$, $h_1$, $n_0$, $n_1$), and galaxy inclination, *i*. This mean ambient density, $<n(HI)> = <N(HI)>/d$, can be compared with $n_{eff}$ to obtain some estimate of the "completeness" of each shell.

We define the parameter, $\beta = n_{eff}/<n(HI)>$, as a measure of shell completeness. Although it is conceivably possible to estimate $\beta$ via pixel-by-pixel comparison of data and model, the simple definition we adopt should help to identify substantially incomplete structures. Perfectly matched shell models in a uniform disk environment would yield values of $\beta \sim 1$. Variations from $\beta = 1$ could arise due to various reasons: (1) only fragments of the shell are present; (2) there are substantial non-uniformities in the shell environment on scales of $R_0$; or (3) the shell model is an imperfect match to the observed HI structure.

Generally, small values of $\beta$ imply increasingly incomplete or poorly matched shell structures in the data. This quantity can therefore be used to isolate the highest quality detections from a continuous distribution of lower quality (although significant) fits to expanding structures within an HI datacube.

## 3. Results: HI shells in NGC 2403

### *3.1. Caveat*

We are still improving our shell detection and characterization package, but at this stage the method is sufficiently refined to

**Table 1.** Properties of NGC 2403

| Attribute | Value | Unit |
|---|---|---|
| Right Ascension (B1950) | 07 32 01.20 | h m s |
| Declination (B1950) | +65 42 57.0 | deg ′ ″ |
| Assumed Distance[a] | 3.3 | Mpc |
| Hubble Type | Sc | |
| Inclination | 62 | ° |
| Position Angle | 125 | ° |
| Total HI Mass[b] | $3.6\times10^9$ | $M_\odot$ |
| H$\alpha$ Luminosity[c] | $7.4\times10^{40}$ | erg $s^{-1}$ |
| Star Formation Rate | 0.66 | $M_\odot$ $yr^{-1}$ |
| $L_B$ | 4.7 | $10^9$ $L_\odot$ |

[a] Sandange & Tammann (1968)
[b] Braun (1995)
[c] Kennicutt et al. (1994)

**Table 2.** HI observations of NGC 2403

| Attribute | Value | Unit |
|---|---|---|
| VLA Configurations | B, C, D | |
| Beam Size, FWHM | 9 | ″ |
| Spatial Resolution | 144 | pc |
| Velocity Resolution | 6.2 | km $s^{-1}$ |
| RMS Noise Level | 1.2 | mJy $beam^{-1}$ $chan^{-1}$ |
| HI Mass Sensitivity | $1.6\times10^4$ | $M_\odot$ |
| Channel Spacing | 5.16 | km $s^{-1}$ |
| Velocity Range | 299 | km $s^{-1}$ |
| Number of Channels | 58 | |

present initial results for NGC 2403. Our main goal here is to demonstrate the application of our cross-correlation technique. The final parameterization of NGC 2403's supershell population may change as our method is refined, especially when we are able to incorporate the predictions of hydrodynamic modeling.

### *3.2. Background, observations, and data reduction*

We first applied our automated package to the moderately-inclined, relatively gas-rich spiral NGC 2403. This galaxy is one of 11 systems included in a recent high resolution 21-cm VLA survey of nearby spirals conducted by Braun (1995, 1997). Table 1 presents relevant properties for NGC 2403. NGC 2403 was chosen as the first galaxy in our study because it has a distance and inclination typical of our sample.

The neutral hydrogen observations used in this project were obtained between March 1989 and November 1990 using the VLA's B, C, and D configurations[1]. The spectral-line cube processed using our automated package was a slightly smoothed version of the full resolution data. In particular, a circular beam of FWHM $\sim$ 9" provided spatial resolution of $\sim$ 140 pc. Individual channel-maps were separated by 5.16 km $s^{-1}$ and the effective velocity resolution was 6.2 km $s^{-1}$ (since on-line Hanning smoothing was used at the VLA). Table 2 gives more information regarding the observations and reduction. See Braun (1995) for a complete description of the reduction procedure.

[1] The National Radio Astronomy Observatory is a facility of the National Science Foundation operated under cooperative agreement by Associated Universities, Inc.

**Table 3.** Narrow-band imagery of NGC 2403

| Attribute | Value | Unit |
|---|---|---|
| Telescope | Burrell Schmidt | |
| Camera and detector | TEK 512 | |
| Filters used | H$\alpha$, red continuum | |
| Central Wavelengths | 6563, 6649 | Å |
| Bandwidth | 75, 75 | Å |
| Pixel Size | 2.6 | ″ |
| Field of View | 22 | ′ |
| Exposure Time | 3×400, 3×400 | sec |

For a comparison between our HI shell catalog and the HII regions of NGC 2403, we obtained narrow-band, continuum-subtracted H$\alpha$ images at KPNO using the Burrell Schmidt and 0.9-m telescopes. Only images from the Schmidt telescope are included in this paper. A full description of these data is given elsewhere (Greenawalt & Walterbos, in prep). Table 3 gives relevant information for these data.

### *3.3. Parameter space survey*

Our HI shell catalog for NGC 2403 was produced using a variety of assumptions for disk scale height, ambient density, and gas velocity dispersion. In particular, 6 variations of the plane-stratified disk model were considered. Observed shell structures were individually matched to a particular parameter set using our significance ranking procedure to identify the best-fitting model. We hoped to learn which assumptions best matched the true gas distribution and furthermore determine how sensitive the shell catalog was to changes in our ambient model. The parameter sets included in our investigation are shown in Table 4.

We searched for HI shells using a total of 150 different filter kernels per ambient disk variation. The kernels specified the appearance of model supershells with in-disk radii, $R_0$, in the range 50-750 pc and in-disk expansion velocities, $V_0$, between 3 and 56 km $s^{-1}$. We also allowed for "stalled" structures by including an ensemble of kernels with $V_0$ = 0.1 km $s^{-1}$. Shells with $R_0$ = 50 pc would be unresolved in our data, but could appear as point-like spikes contiguously extended in velocity (over a range $\sim$2 $V_0$). Table 5 presents details regarding our parameter space survey. The specified range in shell age, $t_7$, excludes stalled shell models.

In selecting how to vary the plane-stratified ambient disk, we chose values of ($h_0$, $h_1$, $n_0$, $n_1$) forcing substantially different predicted shell signatures in every case. Nevertheless, we

**Table 4.** Ambient disk variations

| Scenario Name | $h_0$ (pc) | $h_1$ (pc) | $h_1/h_0$ | $n_0$ ($cm^{-3}$) | $n_1$ ($cm^{-3}$) | $n_0/n_1$ | $\sigma_{shell}$ (km $s^{-1}$) | $\sigma_{dense}$ (km $s^{-1}$) | $\sigma_{diffuse}$ (km $s^{-1}$) | % |
|---|---|---|---|---|---|---|---|---|---|---|
| Nominal, "compact" | 100 | 400 | 4 | 1.0 | 0.3 | 3.33 | 10.0 | 5.0 | 5.0 | 14.7 |
| Starburst, "fluffy" | 100 | 800 | 8 | 1.0 | 0.3 | 3.33 | 10.0 | 5.0 | 5.0 | 22.4 |
| Starburst, "fluffy", low disp. | 100 | 800 | 8 | 1.0 | 0.3 | 3.33 | 1.2 | 1.2 | 8.9 | 32.0 |
| Dense-Envelope | 100 | 400 | 4 | 1.0 | 0.6 | 1.67 | 10.0 | 5.0 | 5.0 | 3.8 |
| Weak-potential | 200 | 800 | 4 | 1.0 | 0.3 | 3.33 | 10.0 | 5.0 | 5.0 | 18.6 |
| Spherical | $\infty$ | – | – | 1.0 | – | – | 10.0 | 5.0 | 5.0 | 8.3 |

**Table 5.** Parameter space survey for HI shells in NGC 2403

| Attribute | Description | Value | |
|---|---|---|---|
| $R_0$ | In-plane radius | 50, 100, ... 750 | pc |
| $V_0$ | In-plane expansion velocity | 0.1, 3, 5, 7, 10, 14, 20, 28, 40, 56 | km $s^{-1}$ |
| $t_7$ | Shell age | 0.5–147 | Myr |

attempted to make each parameter set describe a realistic physical scenario.

As shown in Table 4, we tried both a "compact" and "fluffy" diffuse disk for $h_0$=100 pc. The compact arrangement ($h_1/h_0$=4) is thought to be typical of our galaxy sample. The fluffy diffuse disk ($h_1/h_0$=8) represents how the vertical gas distribution might change in a galaxy experiencing vigorous star formation. For this reason, we labeled it the "starburst" case. After obtaining good results with our "fluffy" disk model, we tried a similar "fluffy" variation in which the gas was assigned an intrinsically low velocity dispersion. In a sample of 11 spirals, including NGC 2403, Braun (1997) demonstrates that the intrinsic line profiles of high brightness HI in galactic disks are characterized by a narrow core with less than 6 km $s^{-1}$ FWHM superposed on faint, but broad Lorentzian wings with 30 km $s^{-1}$ FWHM. Braun's evidence suggests that the dense atomic disk should have a rather low velocity dispersion (corresponding to a kinetic temperature of about 150 K), while only the diffuse atomic disk has a higher dispersion (corresponding to 8000 K) and high observed linewidths are a direct consequence of local expansion signatures. In order to test this hypothesis, we assumed a velocity dispersion of 1.2 km $s^{-1}$ for both swept-up gas and the dense disk while taking $\sigma_{diffuse}$ = 8.9 km $s^{-1}$ for the diffuse disk layer. We refer to this set of supershell models as the "low dispersion, starburst" case. Our "dense-envelope" scenario used the same disk thickness and velocity dispersion values as the "compact" case, but had only a mild density contrast between dense and diffuse components. We also explored an extended dense/diffuse disk combination having twice the full-thickness as our nominal model, but still with $h_1/h_0$=4. This scenario approximates the vertical gas distribution in a disk of lower mass surface density and was therefore labeled as the "weak-potential" case. Finally, we searched for purely-spherical shells in a model ambient disk characterized by uniform density. We did not expect to find extremely large spherical shells, but included this case as a check on our other results.

The predicted model structure derived for shells having identical in-plane radii and expansion velocities was very sensitive to the choice of ambient disk parameters for two reasons: (1) shells either have more room to grow while contained by layers of ambient gas, or (2) the velocity discontinuity allowed at the interface between dense and diffuse layers differs because of a change in the assumed density contrast, $n_0/n_1$. Changes in structure brought about by large full-thickness values (reason 1) typically include either a more complete out-of-plane lobe in both "starburst" cases or reclassification of the shell morphology for a given $R_0$ in our "weak-potential" scenario. That is, for an ambient disk having twice the vertical scale of our "compact" disk, large shells can remain roughly spherical for a longer time and "mushroom-like" shells grow substantially larger before disk break-out. Although important, the changes in model structure associated with the second reason noted above are not as obvious in terms of shell morphology. For the "dense-envelope" case, a decrease in the magnitude of the velocity jump experienced by the expanding shell (at $R_I$), leads to "mushroom" shells more severely confined than identically parameterized counterparts in the nominal ("compact") disk scenario. Furthermore, maximum projected velocities associated with these shells are reduced by a significant factor.

Each disk model interprets the observed HI structure in a somewhat unique manner, leading to a different parameterization of the data's invariant shell population. Noting the fraction of shells best-matched by each parameter set, we constrained properties of the actual HI distribution. The final column in Table 4 indicates the percentage of all detections above a specified significance level, $T_{cat} = 6\sigma$, associated with each disk variation. In total, there were 156 shell detections exceeding the $T_{cat}$ limit – most of these were picked up at some level

by more than one global parameter set. The numbers in Table 4 clearly show that the "low dispersion, starburst" case was most successful in modeling NGC 2403's HI shell population. Nearly 1/3 of the structures in our catalog were best-matched by this ambient model. We interpret this result as further evidence supporting the hypothesis that the dense atomic disk is characterized by cool, low dispersion gas as noted by Braun (1997). Our ordinary "starburst" and "weak potential" scenarios ranked a fairly distant second and third. Accounting for less than 10% of the significant detections, both the purely spherical and "dense-envelope" assumptions were clearly mismatched to our data.

We conclude that a diffuse component of the neutral gas layer in NGC 2403 extends to at least z $\sim$ 400 pc and that the dense disk is likely composed of structures having a small intrinsic velocity dispersion. Information regarding the vertical extent of the dense, inner layer is not as conclusive since the ordinary "starburst" and "weak-potential" assumptions (corresponding to full widths of 100 and 200 pc) produced quite similar shell catalogs.

It is important to note that our package makes it easy to rederive shell characteristics at any later time if more accurate information regarding the ambient gaseous environment becomes available.

### *3.4. Selection of significance*

Our automated object recognition package is effective at detecting complete *and* fragmentary structures. As indicated in Sect. 2.5–2.6, we can impose strict significance and "shell completeness" thresholds to isolate only the highest-quality HI shells from a continuous distribution of 156 complete and fragmentary detections. In the discussion below, it was convenient to select the 50 shells of highest quality by demanding a signal-to-noise ratio $\geq T_{cat}$ = 6 and $\beta \geq \beta_{cat} = 10^{(a-b\sigma)}$, where $a$ = 0.55 and $b$ = 0.1. The constant $b$ was determined by matching the slope of a line connecting the most-complete detections of high significance. The constant $a$ was fixed by our (arbitrary) choice to isolate only 50 high-quality shells. Of these detections, 22 were "best-fit" by velocity projected shell models with $V_0 \geq 3$ km s$^{-1}$. All remaining high-quality detections lacked a detectable expansion signature and appear to be "stalled".

Adopting a shell completeness cutoff guarantees that all cataloged ("high-quality") detections are reasonably well-matched to one of the parameterized supershell models we used for datacube cross-correlation. In any case, it seems unrealistic to demand a perfectly matched cross-correlation kernel (due to potential fragmentation and model inaccuracies – eg. disregard of differential shear and pressure loss upon breakout). Fig. 9 illustrates the distribution of $\beta$ as a function of signal-to-noise in our original (unrestricted) list of 156 significant detections. We also plot the adopted $\beta_{cat}$ threshold. Significant detections falling below this cutoff are categorized as being structurally incomplete, perhaps due to fragmentation. These incomplete shells are likely an important constituent of the diffuse atomic ISM, contributing a "frothy" character to the HI in NGC 2403.

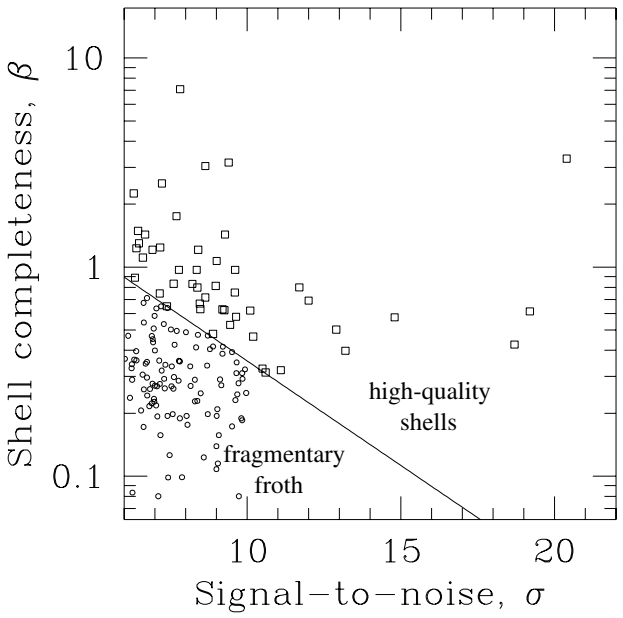


**Fig. 9.** Shell completeness. as measured by $\beta$, varies continuously over a wide range in our unrestricted list of significant shell detections, reflecting the fact that we observed both fragmentary structures and "complete" shells in environments of varied ambient density. This plot, showing $\beta$ versus signal-to-noise, excludes a few high $\beta$ detections. We have indicated our adopted $\beta_{cat}$ threshold with a solid line.

Our HI shell catalog is certainly not complete. We are limited by sensitivity, spatial resolution, crowding, and the assumptions built into our computation of cross-correlation kernels. The most severe of these limitations is sensitivity. In particular, small shells forming in relatively low density environments are difficult to detect. The position-dependent RMS fluctuation level ($S_{RMS}$) of a cross-correlated, high-pass filtered datacube varies as a function of $R_0$ and the amount of observed emission in the original data. By imposing a catalog significance threshold ($T_{cat}$) we allow shells of given $R_0$ only if they exceed a well-defined limiting HI mass,

$$M_{limit} = 2.4 \text{ x } 10^5 \left(\frac{D}{\text{Mpc}}\right)^2 \left(\frac{\Delta v_{ch}}{\text{km s}^{-1}}\right) T_{cat} S_{RMS} \, M_\odot \qquad (11)$$

Although $M_{limit}$ is well-defined, it does vary from shell-to-shell since $S_{RMS}$ is a measure of the *local* RMS fluctuation in the vicinity of each detection. Fig. 10 presents a plot showing $(M_{HI})_{obs}$ versus $R_0$ for 156 detections above 6$\sigma$, but having any $\beta$. Also plotted is a 2nd order polynomial fit to the $M_{limit}$ values associated with these detections. We find that $M_{limit}$ increases almost linearly with $R_0$. Perfectly matched shells which happen to form in exceptionally low density environments will be excluded from our shell catalog if $(M_{HI})_{obs} \leq M_{limit}$.

Spatial resolution limits catalog completeness only for small shells. We minimized the number of structures missed in this manner by convolving our cross-correlation models to account for the finite beam size. Rather than causing relatively small shells to remain undetected, spatial resolution more significantly

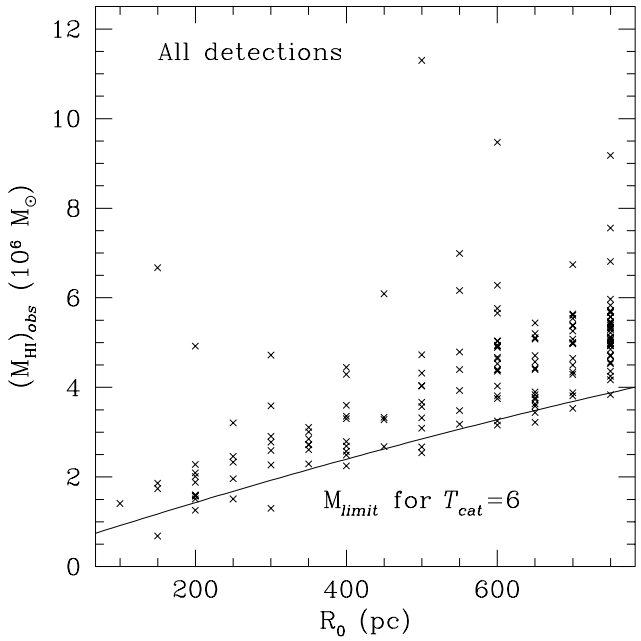


**Fig. 10.** $(M_{HI})_{obs}$ versus in-plane shell radius, $R_0$. Although not plotted, each detection has an associated value of $M_{limit}$. We use the position-dependent RMS fluctuation level in a cross-correlated, high-pass filtered datacube to determine $M_{limit}$ with Eq. (11). The solid line is a fit to individual values of $M_{limit}$ over the sampled range in $R_0$. Observed emission structures perfectly-matched to a model supershell signature are only included in our catalog if they have a detected mass exceeding $M_{limit}$. This is a consequence of the fact that we require detections to be highly significant ($T_{cat}$=6).

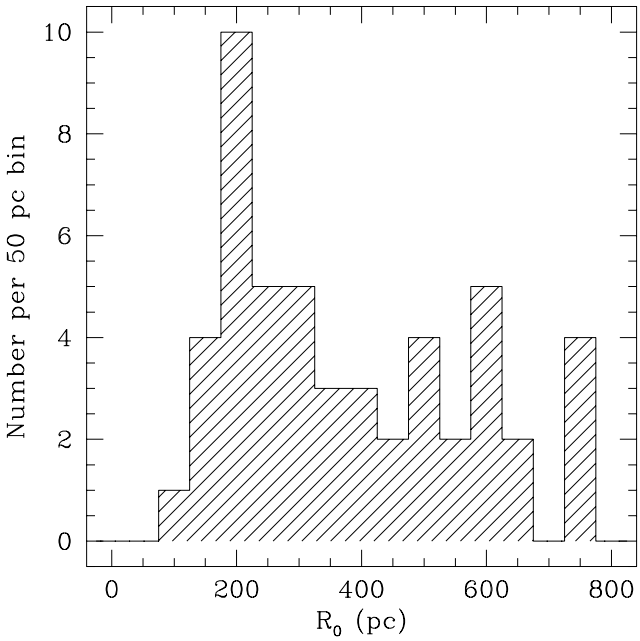


**Fig. 11.** Observed $R_0$ distribution for the 50 high-quality HI shells found in NGC 2403. We suffer from incompleteness due to sensitivity at small $R_0$.

complicates shell classification in terms of $R_0$. That is, we still detect small, beam-smoothed structures but find it difficult to accurately characterize their properties because shells with small $R_0$ all "look alike".

The effect of shell-shell crowding on catalog completeness is an issue we are still investigating. Simulations similar to those used in Sect. 2.5 for fine-tuning our significance ranking procedure will be employed to study the effects of cross-correlation analysis on shell pairs.

Finally, we are aware that our analytic modeling of shell expansion becomes inaccurate when shells grow large. Future refinements to our automated package, such as hydrodynamic modeling, should rectify this problem. At present, the fact that we allow structures having $\beta \geq \beta_{cat}$ helps to include real shells for which our model is not perfectly suited.

In Fig. 11, we plot the observed distribution of shell radius for our sample of high-quality shells in NGC 2403. Incompleteness at small $R_0$ is apparent. Simulations involving the recovery of inserted shell signatures from a real datacube can be used to gain a better understanding of incompleteness due to sensitivity limits. We completed testing of this nature for 3 in-plane expansion velocities, $V_0$ = 5, 14, and 40 km $s^{-1}$; and 4 in-plane radii, $R_0$ = 100, 300, 500, and 700 pc. In each case, artificial shells were inserted assuming nominal density ($n_0$ = 1 $cm^{-3}$, $n_1$ = 0.3 $cm^{-3}$) and the density at which real shells of each size were most commonly found. Furthermore, we also tried inserting shells at 75, 50, and 25% of this benchmark density. In the case of $R_0$ = 100 pc, we included density estimates from slightly larger shells since only one high-quality shell having $R_0$ = 100 pc was detected.

Tables 6–9 show the results of our shell recovery simulations. Each table pertains to the given value of $R_0$ and presents the percentage of shells recovered as a function of $V_0$ and assumed density. We note the following points: (1) Only for $R_0 \gtrsim 300$ pc, do we detect structures formed in a nominal density environment with $n_0$ = 1. (2) Shells with $R_0$ = 100 pc can only be detected if the ambient density is elevated by a factor approaching one order of magnitude. (3) Decreasing $R_0$ by 200 pc is usually enough to make shells undetectable if they remain in a region of comparable density. (4) Most shells included in our catalog would not have been detected if they had evolved in an environment with ambient density reduced by a factor of 2. Clearly, sensitivity is an issue of extreme importance when interpreting HI shell catalogs. Unfortunately, it is not possible to derive an accurate sensitivity correction factor without being able to specify the probability of shell formation in environments of varied density. We likely detect less than 1 out of 20 shells in the regime $R_0 \leq 100$ pc. However, based on estimates of n(HI) derived from column density measurements, it seems that we should be complete within a factor of 2 for shells with $R_0 \gtrsim 300$ pc.

**Table 6.** Percentage of model shells recovered for $R_0$ = 700 pc.

| | $n_{0,ins}$ (cm$^{-3}$) | | | | |
|---|---|---|---|---|---|
| $V_0$ | 1.00 | 0.20 | 0.15 | 0.10 | 0.05 |
| 5 | 100 | 100 | 88 | 0 | 0 |
| 14 | 100 | 100 | 12 | 0 | 0 |
| 40 | 100 | 76 | 0 | 0 | 0 |

**Table 7.** As in Table 6, except $R_0$ = 500 pc.

| | $n_{0,ins}$ (cm$^{-3}$) | | | | |
|---|---|---|---|---|---|
| $V_0$ | 1.00 | 0.32 | 0.24 | 0.16 | 0.08 |
| 5 | 100 | 100 | 35 | 0 | 0 |
| 14 | 100 | 100 | 47 | 0 | 0 |
| 40 | 100 | 100 | 24 | 0 | 0 |

**Table 8.** As in Table 6, except $R_0$ = 300 pc.

| | $n_{0,ins}$ (cm$^{-3}$) | | | | |
|---|---|---|---|---|---|
| $V_0$ | 1.00 | 0.90 | 0.68 | 0.45 | 0.22 |
| 5 | 100 | 100 | 94 | 6 | 0 |
| 14 | 100 | 100 | 88 | 6 | 0 |
| 40 | 100 | 82 | 6 | 0 | 0 |

**Table 9.** As in Table 6, except $R_0$ = 100 pc.

| | $n_{0,ins}$ (cm$^{-3}$) | | | | |
|---|---|---|---|---|---|
| $V_0$ | 13.0 | 9.75 | 6.50 | 3.25 | 1.00 |
| 5 | 100 | 94 | 6 | 0 | 0 |
| 14 | 94 | 59 | 0 | 0 | 0 |
| 40 | 0 | 0 | 0 | 0 | 0 |

### *3.5. Shell characteristics*

The shells included in our catalog are characterized by the mean and median properties indicated in Table 10. For reference, we also list the maximum and minimum values of each catalog variable. Notice that the mean radius for stalled shells is larger than for those still expanding. Stalled shells become most prominent at radii $\geq$ 300 pc.

In Fig. 12, we present logarithmically binned histograms for *expanding* HI shells within NGC 2403. "Stalled" structures are not included. In each panel, we plot the distribution of interest for 22 high-quality shells (the densely-hatched histogram) and also for the unrestricted catalog (shells of any $\beta$). This allows a check for agreement between "complete" shells and the more fragmentary structures detected by our shell recognition package. Fig. 12a shows the distribution of $(M_{HI})_{obs}$. The plot

**Table 10.** Properties of high-quality shells in NGC 2403

| Expanding Shells (22) | | | | | |
|---|---|---|---|---|---|
| Variable | Unit | Mean | Median | Min | Max |
| $R_0$ | pc | 280 | 200 | 100 | 750 |
| $V_0$ | km s$^{-1}$ | 23 | 20 | 3 | 56 |
| $(M_{HI})_{obs}$ | $10^6$ M$_\odot$ | 3.5 | 2.3 | 0.7 | 21 |
| $(E_k)_{obs}$ | $10^{51}$ erg | 100 | 26 | 0.6 | 830 |
| $t_7$ | $10^7$ yr | 2.2 | 1.1 | 0.1 | 9.8 |
| $N_*$ | | $4.8\times10^3$ | 410 | 1.4 | $4.7\times10^4$ |
| Stalled Shells (28) | | | | | |
| Variable | Unit | Mean | Median | Min | Max |
| $R_0$ | pc | 460 | 500 | 200 | 750 |
| $(M_{HI})_{obs}$ | $10^6$ M$_\odot$ | 4.8 | 4.6 | 1.5 | 11 |

indicates observed HI shell masses are generally quite similar, lying in the range 2–5$\times10^6$ M$_\odot$. A few shells are detected with $(M_{HI})_{obs}$ almost an order of magnitude lower and one shell is found having $(M_{HI})_{obs} \sim 2\times10^7$ M$_\odot$. Our $(M_{HI})_{obs}$ values are consistent with the largest HI shell masses estimated for M31 and M33, by Brinks & Bajaja (1986) and Deul & den Hartog (1990) respectively. In contrast to the results of Kamphuis (1993) for M101, we almost never find expanding shells with $(M_{HI})_{obs}$ greater than $10^7$ M$_\odot$. Panel (b) of Fig. 12 presents the distribution of kinetic energy for HI shells detected in NGC 2403. For high-quality shells the distribution is essentially flat over the range $(E_k)_{obs}$ = $10^{51}$–$10^{54}$ erg. Kinetic energies of this magnitude can be attributed to typical OB associations. The lack of a significant peak in the $(E_k)_{obs}$ distribution may reflect incompleteness at low energies. We find that the distribution for our unrestricted catalog *is peaked* near $(E_k)_{obs}\sim 3\times10^{51}$ erg and declines significantly toward increasing energy. Fig. 12c presents the dynamical age distribution of all detected shells. Our $\beta$ cutoff tends to exclude the oldest and most massive (see Panel a) shells from our high-quality catalog. This is desirable since the assumptions of our shell expansion model start to break down for large $t_7$. Although it is tempting to interpret the observed $t_7$ distribution as evidence for claims regarding the history of star-formation/shell-creation in NGC 2403, we refrain from such analysis since shells of different ages may not have equal detection likelihood. The observed distribution of $N_*$ is presented in Fig. 12d. The shells in our unrestricted sample require progenitor clusters containing between 1 and $\sim 10^4$ stars with M $\geq$ 7 M$_\odot$. We hope to confirm the $N_*$ data presented in Fig. 12d using multi-color photometric analysis of the stellar populations inside typical HI shells.

Another issue we can address is the observed dependence of kinetic energy on age for HI shells. Fig. 13 shows a plot of these variables for all high-quality, expanding structures. "Stalled" superbubbles are excluded since their age is not well-determined. The plot indicates that we detect older HI shells with systematically lower kinetic energy than young shells. We do not detect

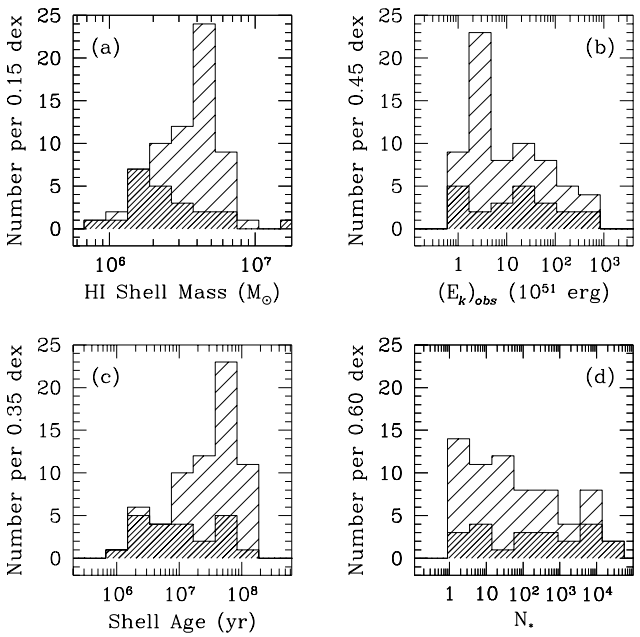


**Fig. 12a–d.** Logarithmically binned histograms showing various properties of expanding HI shells in NGC 2403. Specifically, we plot: **a** observed HI shell mass, **b** shell kinetic energy, **c** dynamical age, and **d** $N_*$, the number of stars originally formed with M$>$ 7 $M_\odot$ in a shell's progenitor association. For each panel we plot the data pertaining to *all* expanding shells with a sparsely-hatched histogram. Likewise, the densely-hatched histogram describes only the 22 high-quality, expanding structures.

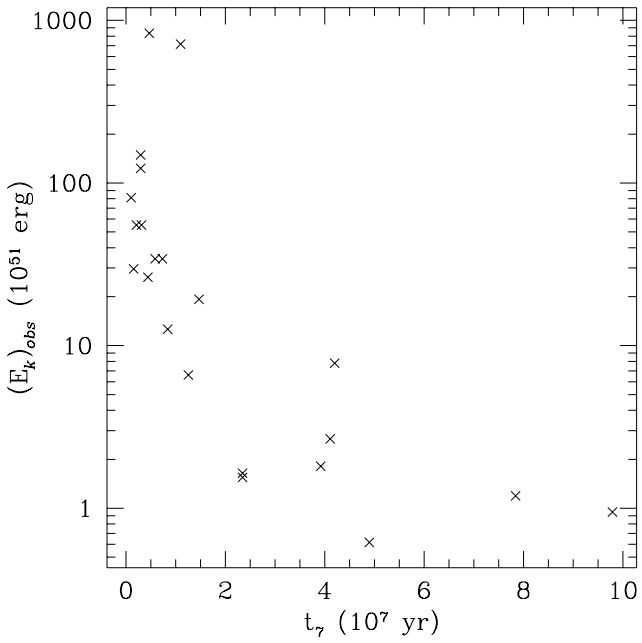


**Fig. 13.** $(E_k)_{obs}$ versus $t_7$, dynamical shell age. This plot suggests that HI shells may dramatically lose kinetic energy as they become old. The decline appears to halt by $t_7$∼5. A potential explanation for such energy loss is the venting of pressure experienced by supershells as they break out of the galactic disk. In the text, we discuss other systematic influences and selection effects.

an initial rise of $(E_k)_{obs}$ at dynamical times smaller than $\sim$ 5 Myr, but after this time observed kinetic energies decline over 2 orders of magnitude during the next $\sim$ 40 Myr. By $t_7 \sim 5$, $(E_k)_{obs}$ ceases to drop any further. What causes the observed dependence of $(E_k)_{obs}$ on $t_7$? Is this merely a consequence of various selection effects or might it reflect an intrinsic evolutionary sequence in the kinetic energy of neutral gas associated with supershells?

One aspect of the observed distribution can clearly be attributed to a selection effect; namely our limited mass sensitivity, in particular for small radii (and hence young shells), as illustrated in Fig. 10. This leads quite naturally to an absence of young shell detections with low kinetic energy in Fig. 13. The absence of old, high energy shells cannot be accounted for in this way. One possibility that comes to mind is that high energy supershells may occur preferentially in more complex environments, so that older objects are more likely to be confused or even physically dispersed by subsequent generations of star formation. However, our data do not strongly support this conclusion. Only 5 of 13 detections having $(E_k)_{obs} \geq 10^{52}$ ergs are found in extremely active star-forming areas of the galaxy. Another possibility is that our supershell expansion model provides a systematically poorer fit to old shells relative to young. At some level we realize that this bias must be present, if for no other reason than because departures from cylindrical symmetry are likely to be much greater at later times. More importantly, the limitations of our analytic expansion model (in particular the assumption of negligible pressure venting) may result in a systematic misclassification of older shells. We can at least partially address this concern by noting that the shell completeness parameter, $\beta$, only declines by a factor of 3 for most shells from $t_7$ = 0 to 6. It seems unlikely that that the entire decline in detected shell kinetic energy is due to this effect.

Assuming that the trend seen in Fig. 13 is at least partially due to a real evolutionary effect, we can consider which physical mechanism might be responsible for such a decline. One possibility is that we are detecting the decline of mechanical luminosity associated with aging supershell progenitor clusters. As noted in Sect. 2.2, our models assume constant energy input over the lifetime of a shell. In point of fact, this is not true. Incorporation of more realistic shell models may help us to clearly discern a mechanical energy cutoff. We suspect that the venting of gas pressure associated with disk blowout is another likely mechanism for the apparent decline of $(E_k)_{obs}$. If large portions of the old structures included in Fig 13 have already expanded beyond the limits of the diffuse HI layer, our estimates of $(E_k)_{obs}$ would be systematically lower than the total kinetic energy, $(E_k)_{tot}$, for such shells since we measure the energy of neutral gas only. Most of a blowout shell's kinetic energy would be in the ionized, high-velocity flow leaving the disk. Consequently, the actual distribution of $(E_k)_{tot}$ may be relatively flat, in contrast to that of $(E_k)_{obs}$ shown in Fig. 13.

Our current catalog of supershells in NGC 2403 also supports the following statements: (1) Only a few of the large-scale

integrated HI minima, which give column density maps their overall "swiss-cheese" appearance, are identified as actively expanding (or even stalled) shells. Most of these regions appear to be only inter-arm gaps in the HI distribution. It will be interesting to apply our automated algorithm to 21-cm datacubes which have already been surveyed for HI shells in a visually-based manner (M31: Brinks & Bajaja (1986), M33: Deul & den Hartog (1990), HoII: Puche et al. (1992), M101: Kamphuis (1993), SMC: Staveley-Smith et al. (1997)). Some of these studies have identified large expanding shells coincident with integrated HI minima. Our shell recognition package should be able to confirm such detections and accurately characterize their properties. (2) Cataloged shell positions extend nearly to the edge of the neutral gas disk. The surface number density of shells appears regulated by average HI column density with enhancements in regions having elevated star formation. This is not a selection effect at least for regions of typical integrated HI column – the $\beta_{cat}$ acceptance condition provides equal detection efficiency in environments of varied column density, since $\beta$ is determined on a shell-by-shell basis using a local estimate of the ambient gas density derived from our N(HI) map. In regions of extraordinarily low ambient density, we are ultimately limited by sensitivity (see the $M_{limit}$ discussion of Sect. 3.4). Below we return to this topic in a more quantitative fashion. (3) Shell size does not correlate with galactocentric radius. (4) Most of the shells located in the extreme periphery of the galaxy ($R_g \geq 10$ kpc) have been characterized as stalled or slowly expanding supershells.

As mentioned above, the surface number density of shells (within the galaxy plane) appears regulated by the local average HI column density and rate of massive star formation. Fig. 14 helps to more clearly illustrate this effect. We have plotted the normalized surface number density of high-quality shells as a function of galactocentric radius. For comparison we also show the azimuthally-averaged HI column density and H$\alpha$ surface brightness (each normalized to a peak of unity). It seems that supershells form most frequently in regions having significant HI and locally enhanced star formation. The dependence on HI column density cannot be a selection effect since catalog membership is determined by our $\beta$ criterion. Significant discrepancy between the mean HI column density and the anticipated surface number density of shells is observed in the galaxy center. We detect fewer shells in the center of NGC 2403 than one might naively expect based on the radial distribution of HI gas and HII regions. We can think of several reasons to explain this result: (a) The inner portion of the galaxy might actually be extremely active and filled with expanding, but often-overlapping structures. The confused nature of sub-kpc HI kinematics in this region would then make it difficult to recover those shells which are truly present. (b) Our shell models do not include shear arising from differential galactic rotation. Shear will be most prominent *just outside* the co-rotation radius of a spiral galaxy, indicating that our filter kernels may be poorly matched to supershell structure in these areas. It is conceivable that our catalog misses supershells being torn apart by differential rotation, with the largest fraction remaining undetected in the inner regions of NGC 2403. (c) Shells might be more evident in molecular gas. (d) Shells might be very small in high density environments.

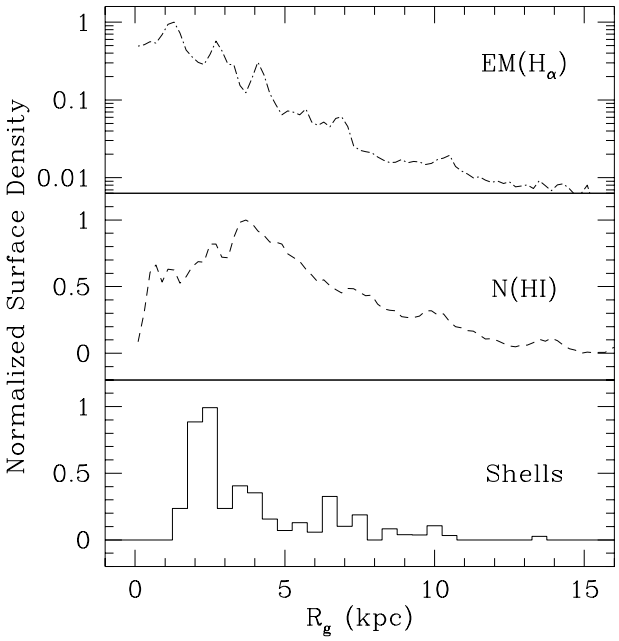


**Fig. 14.** Normalized surface number density for 50 high-quality HI shells as a function of galactocentric radius. We also plot the azimuthally-averaged HI column density and H$\alpha$ surface brightness, normalized to a maximum of unity. Notice the excellent correspondence between peaks in the mean H$\alpha$ emission measure and the surface number density of shells. Furthermore, in the presence of massive star formation, the maximum surface number density of shells appears regulated by the radial variation of N(HI).

The 50 high-quality shells in our catalog account for a total of $2.1\times10^8$ $M_\odot$ of HI. Collectively, they represent at least $2.2\times10^{54}$ erg of kinetic energy. We derive a surface covering factor of 5% percent for intact, detectable shells in the disk of NGC 2403. Including fragmentary structures, the estimate rises to $\sim$ 25%. The total HI mass of complete shells and fragmentary structures is $6.7\times10^8 M_\odot$, roughly 1/5 of the neutral atomic hydrogen in NGC 2403.

### *3.6. HI shells and star-forming regions*

We have selected 4 shells from our NGC 2403 catalog in order to demonstrate how results from our automated object recognition package can constrain the time-dependent relation between neutral bubbles and HII regions. A complete analysis of this kind will be included in subsequent papers.

Qualitatively, significant ionizing radiation is only expected from very young, massive shell-powering clusters in which O and B stars remain on the main sequence. This reasoning implicitly assumes a single burst of coeval star formation. The evolutionary synthesis models of Leitherer & Heckman (1995) predict the flux of Lyman continuum photons, $N_{Lyc}$, associated with an instantaneous starburst. They show $N_{Lyc}$ drops from an initial maximum by almost three orders of magnitude be-

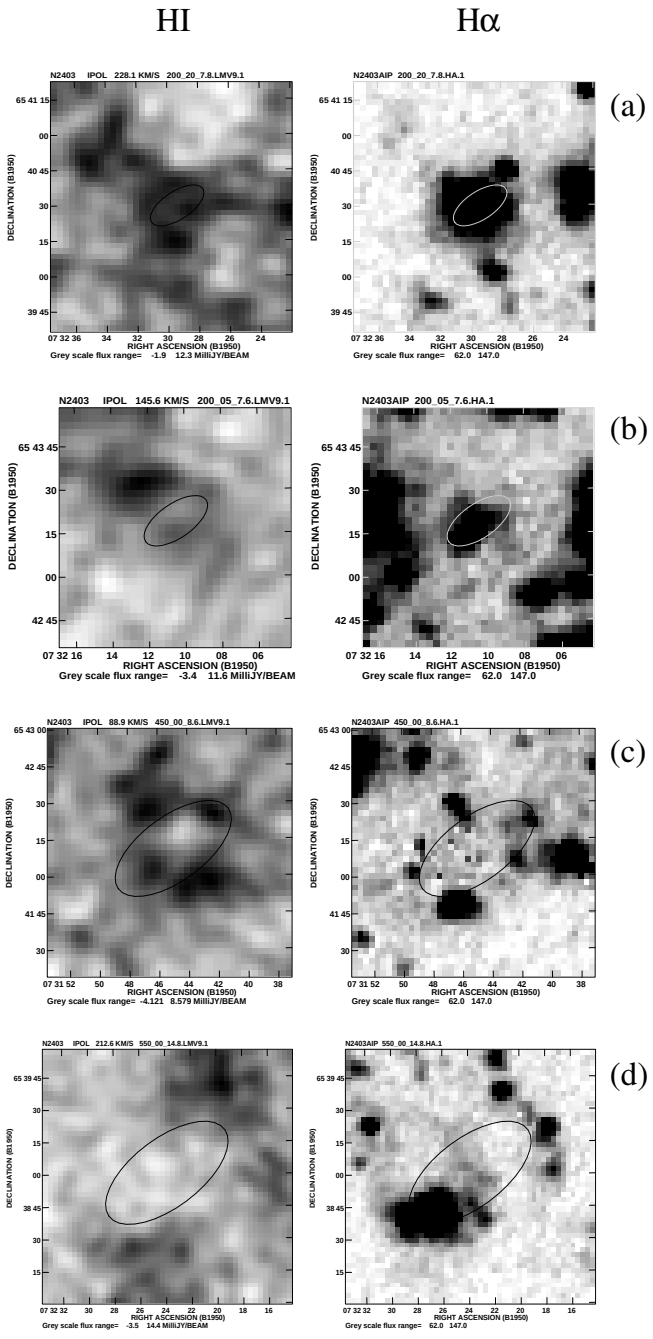


**Fig. 15a–d.** Four HI supershells located in NGC 2403. Each panel contains two image subsections centered on a detected structure. We include a channel-map associated with the shell rest velocity and a continuum-subtracted H$\alpha$ image. In panels **a** and **b**, we depict expanding shells having $R_0$ = 200 pc. In panels **c** and **d**, we show two stalled chimneys, with radii of 450 and 550 pc, respectively. The HI cavity outline has been marked in each panel. Note that both young shells contain an HII region, while each large chimney is surrounded by areas of apparent sequential star formation.

fore $t_7 = 1$. Indeed, $t_7 \sim 1$ marks a turning point in the spectral evolution of a massive stellar cluster, with the onset of most supernovae taking place around this time. Metal-rich clusters would evolve somewhat quicker, but for simplicity we adopt $10^7$ yrs as the greatest elapsed time at which we expect to observe shell photoionization or nebular emission from a shell progenitor association.

Additionally, sequential star formation (SSF) may occur within the gravitationally-unstable, swept-up gas composing old HI shells. The time-scale for this process is rather uncertain, as it depends critically on density in the ambient medium before superbubble formation and potentially on the presence of other large scale gas motions (eg. neighboring shells, differential rotation) acting either as a "trigger" mechanism or slowing down the process. Bodenheimer (1992) indicates sequential star formation might nominally begin at $t_7 = 10$, with the formation of giant molecular clouds occurring by $t_7 = 5$. If giant molecular clouds already exist in the vicinity of an expanding supershell, we suspect sequential star formation might be possible at dynamical ages of only a few times $10^7$ years.

Fig. 15 presents a channel-map subsection and continuum-subtracted H$\alpha$ imagery centered on each of 4 superbubbles. Although we present the rest-velocity HI data for each shell, observed structure is not necessarily most evident in that particular channel. Our 3-D cross-correlation method takes full advantage of all relevant data, including structure present in adjacent channels. An inclination-projected outline of the best-fit inner cavity wall has been appropriately marked in every panel. Our models are cylindrically symmetric, so these outlines are just ellipses aligned to match the position angle of NGC 2403's major axis. Two of the shells shown here have been characterized as actively expanding, while the others are best-matched with stalled chimney models.

Both the relatively young, expanding shells shown in Fig. 15 are centered on regions of strong H$\alpha$ emission, probable progenitor HII regions. Panel (a) shows a superbubble with ($R_0$, $V_0$) = (200 pc, 20 km s$^{-1}$), giving it an age of $\sim$ 6 Myr. In this case, the observed nebular emission is quite expected. Panel (b) depicts a shell of the same size but having $V_0$ = 5km s$^{-1}$, implying an age of 24 Myr. Following the discussion above, we would not anticipate photoionized gas coincident with this structure. It seems likely that this shell is powered by a cluster undergoing non-coeval star formation, since it still has a significant ionized counterpart long after $t_7 \sim 1$. The featured shells require progenitor associations having $N_*$ equal to $\sim$ 400 and 5, respectively.

The large, stalled shells highlighted in Fig. 15 are each surrounded by an incomplete ring of HII regions. For this reason, the visual appearance of both associated H$\alpha$ image subsections is quite suggestive of SSF. The featured chimneys have in-plane radii of 450 and 550 pc, respectively, in panels (c) and (d). Deriving a lower limit on their age by assuming $V_0 \leq 3$ km s$^{-1}$ in Eq. (7), we find that $t_7 \geq 8.8$ and 10.8. These timescales agree nicely with the anticipated period for SSF to occur, given our discussion above. Incidentally, a prominent ionized shell adjoins to the NE of the chimney in Fig. 15d. The expansion

signature of this structure was also detected in HI, although at a significance level just below $T_{cat}$.

As illustrated using the supershells of Fig. 15, understanding the correlation between neutral shells and ionized hydrogen is not a trivial endeavor. We are currently modifying our automated object recognition package to be more precise with regard to the treatment of photoionized gas. The next version of our modeling code will compute the radiative transfer within non-spherical shells, accounting for flux escaping through chimney structures, and will predict an approximate H$\alpha$ luminosity for each neutral shell detection.

On a more global scale, most observed HI shells in NGC 2403 are confined to the disk area populated by HII regions. Neutral shells typically don't appear to form in regions with a low probability of massive star formation. The majority of shells detected in regions devoid of H$\alpha$ emission are extremely large and have evolved in a low density environment (near the outer edge of the HI disk) where SSF might be suppressed. Energetically speaking, we note it would be easier to create supershells in a region of low density. Consequently, the lack of bright HII regions near large outlying shells is not too surprising. Such shells could have been formed by the present-day observed HII region population of the outer disk.

Another way to check the overall correspondence between HI shells and massive star formation is to compare the current star formation rate (SFR) derived from global measurements of the H$\alpha$ luminosity (Kennicutt 1983) with the total SFR implied by $N_*$ values in our shell catalog. We define $<SFR_*>$ as the mean rate of star formation over the period $t_7$=0 to $t_7$=$(t_7)_{max}$, where $(t_7)_{max}$ is the age of the oldest HI shell considered. It is given by:

$$< SFR_* > = \frac{\sum N_{*,k}}{(t_7)_{max}} M_* R_*, \quad (12)$$

where the index k runs over individual HI shells in our catalog, $M_*$ is the average mass of the stars included in the $N_*$ count, and $R_*$ is the ratio of total mass for stars not included in $N_*$ with respect to those counted. In this instance, $M_*$ = 15.7 $M_\odot$ for Kennicutt's assumed IMF and an upper mass limit of 100 $M_\odot$. Using the same IMF, $R_*$ = 5.5.

$<SFR_*>$ essentially measures the formation rate of superbubble progenitor stars required to explain the existence of the observed HI shell population. Considering only high-quality, expanding shells (for which $t_7$ can be accurately derived), we find $<SFR_*> = 1.05\times10^5$ $M_*$ $R_*$ / $(9.79\times10^7$ yr) = 0.09 $M_\odot$ $yr^{-1}$. This result is small compared with the SFR derived from NGC 2403's global H$\alpha$ luminosity, 0.66 $M_\odot$ $yr^{-1}$. However, $<SFR_*>$ is quite sensitive to changes in $(t_7)_{max}$. As an example, $\sim$ 75% of the high-quality, expanding shells detected have dynamical ages less than 25 Myr. Rederiving the implied mean star formation rate for this subset, we find $<SFR_*> \sim 0.38$ $M_\odot$ $yr^{-1}$. We conclude that the steady-state "maintenance" of a substantial supershell population requires mechanical luminosity from $\sim$ 10–60% of the massive stars currently being produced in NGC 2403. It is also possible that the current SFR is elevated with respect to the past $10^8$ years as a whole. If this were true, it is conceivable that supershell formation may account for nearly all available mechanical energy associated with massive stars.

## 4. Summary & future applications

We have identified 22 expanding HI shells in the disk of NGC 2403, with a median in-plane radius of 200 pc and typical in-plane expansion velocity of 20 km $s^{-1}$. Individual shells are usually formed from $\sim$ 2–3$\times10^6$ $M_\odot$ of swept-up HI and have a kinetic energy of $10^{51-53}$ ergs. Together, these shells represent a total HI mass of $7.6 \times 10^7$ $M_\odot$. They are collectively associated with $2.2 \times 10^{54}$ ergs of kinetic energy.

In addition to expanding shells, we detected 28 highly significant structures best-fit by stalled supershell models. The median size of stalled structures, 500 pc, is consistent with their interpretation as chimneys connecting NGC 2403's disk and halo.

As shown in Fig 9, there appears to be a *continuous* transition from largely complete, "high-quality" HI shells to fragmentary structures. We clearly detect a significant number of structures which have a derived completeness in the range of 20 to 40%. We interpret this fact as evidence for a frothy background environment composed partially of shell fragments. These incomplete structures may be the remnants of a supershell population formed during previous epochs of star formation. Slightly less than 1/5 of the entire HI mass of NGC 2403 can be decomposed into a system of such shell fragments which have a contrast of at least 6:1 with respect to the general background structure. During the upcoming analysis of supershell populations in the rest of our galaxy sample, we will look for any trends in the gross properties or location of bubble fragments.

These results for NGC 2403 convincingly demonstrate the utility of our automated method for shell detection and characterization. Shell catalogs produced in this manner should help to better understand differences in the ISM for galaxies of varied morphological type and refine current theoretical ideas of supershell evolution.

We are now in an excellent position to extend systematic analysis of superbubbles to a large sample of galaxies, looking for trends in the total number, spatial distribution, and properties of shells observed in different galaxy types. We will: (1) produce a robust catalog of shells for each galaxy and directly compare observations with a model representation of the shell population, (2) incorporate space-based data regarding the hot ISM and massive stars embedded within HI shells. These data will be used to check the agreement between our estimates of $t_7$ and $N_*$ for each shell and the observed parameters of each embedded stellar population.

In collaboration with S. Mashchenko, we are starting to adapt the robust 3-D numerical models of Silich et al. (1996b) for use in deriving "observable supershell signatures". It is possible that the NGC 2403 HI shell catalog presented in this paper will change somewhat when the data is reanalyzed using a more realistic treatment of supershell evolution. At this stage, our preliminary scientific results should be viewed *principally* as a

demonstration of the datacube cross-correlation object recognition method.

Although we have not stressed the applicability of our automated survey method to spectral line datacubes made at optical wavelengths, another future application of this work will be adapting our technique to process H$\alpha$ cubes. We have already begun acquisition of TAURUS Fabry-Perot datacubes for some of the galaxies in our sample.

*Acknowledgements.* D.A.T. would like to express appreciation to the Netherlands Foundation for Research in Astronomy (NFRA) – much of the package introduced in this paper was developed while D.A.T. was a summer student and visiting scientist in Dwingeloo. D.A.T. is currently funded as part of the NASA Graduate Student Researchers Program (NGT-51640). This project has also been supported by the following grants: NASA ADP NAG5-2426, NSF AST-91-23777, AST-96-17014. The National Radio Astronomy Observatory is a facility of the National Science Foundation operated under cooperative agreement by Associated Universities, Inc.

## References

Bodenheimer, P. 1992, in *Star Formation in Stellar Systems; proceedings of the third Canary Islands Winter School of Astrophysics*, edited by G. Tenorio-Tagle, M. Prieto, F. Sánchez (Cambridge University Press: Cambridge), p.1
Braun, R. 1995, A&AS, 114, 409
Braun, R. 1997, ApJ, 484, 637
Brinks, E., Bajaja, E. 1986, A&A, 169, 14
Deul, E., den Hartog, R. 1990, A&A, 229, 362
Ferrière, K., Mac Low, M., Zweibel, E. 1991, ApJ, 375, 239
Heiles, C. 1976, ApJ, 208L, 137
Heiles, C. 1979, ApJ, 229, 533
Heiles, C., Habing, H. 1974, A&AS, 14, 1
Hindman, J.V. 1967, Aust. J. Phys., 20, 147
Hu, E. 1981, ApJ, 248, 119
Kamphuis, J. 1993, PhD thesis
Kennicutt, R.C. 1983, ApJ, 272, 54
Kennicutt, R.C., Tamblyn, P., Congdon, C., 1994, ApJ, 435, 22
Koo, B., McKee, C. 1990, ApJ, 354, 513
Leitherer, C., Heckman, T. 1995, ApJS, 96, 9
Mac Low, M., McCray, R. 1988, ApJ, 324, 776
Mac Low, M., McCray, R., Norman, M. 1989, ApJ, 337, 141
McCray, R., Kafatos, M. 1987, ApJ, 317, 190
McGee, R.X., Milton, J.A. 1966, Aust. J. Phys., 19, 343
Norman, C., Ikeuchi, S. 1989, ApJ, 345, 372
Oey, M. 1996, ApJ, 467, 666
Puche, D., Westpfahl, D., Brinks, E., Roy, J., 1992, AJ, 103, 1841
Rand, R., Stone, J. 1996, AJ, 111, 190
Rand, R., van der Hulst, J.M., 1993, AJ, 105, 2098
Reynolds, R.J. 1991, in *The Interstellar Disk-Halo Connection in Galaxies, IAU Symposium No. 144*, edited by H. Bloemen (Kluwer: Dordrecht), p.67
Sandage, A., Tammann, G.A. 1968, ApJ, 151, 531
Shull, M., Saken, J. 1995, ApJ, 444, 663
Silich, S., Mashchenko, S., Tenorio-Tagle, G., Franco, J., 1996a, MNRAS, 280, 711
Silich, S., Franco, J., Palous, J., Tenorio-Tagle, G., 1996b, ApJ, 468, 722
Staveley-Smith, L., Sault, R., Hatzidimitriou, D., Kesteven, M., McConnell, D., 1997, MNRAS, 289, 225
Tenorio-Tagle, G., Bodenheimer, P., 1988, ARA&A 26, 145
Tenorio-Tagle, G., Franco, J., Bodenheimer, P., Rozyczka, M., 1987, A&A, 179, 219
Tenorio-Tagle, G., Palous, J. 1987, A&A, 186, 287
Tenorio-Tagle, G., Rozyczka, M., Bodenheimer, P. 1990, A&A, 237, 207
Tomisaka, K., 1992, PASJ, 44, 177
Weaver, R., McCray, R., Castor, J., Shapiro, P., Moore, R., 1977, ApJ, 218, 377
Westerlund, B.E., Mathewson, D.S. 1966, MNRAS, 131, 371

This article was processed by the author using Springer-Verlag LaTeX A&A style file *L-AA* version 3.